Title: Cell-type-specific plasticity in synaptic, intrinsic, and sound response properties of deep-layer auditory cortical neurons after noise trauma

Authors: Yanjun Zhao[1,4,!], Stylianos Kouvaros[1,4,7,!,], Nathan A. Schneider[1,4-6], Rebecca F. Krall[1,4], Stephanie Lam[3], Megan P. Arnold[1,4], Ross S. Williamson[1-6*], and Thanos Tzounopoulos[1,2,4*]

[1]Department of Otolaryngology, University of Pittsburgh, Pittsburgh, PA

[2]Department of Neurobiology, University of Pittsburgh, Pittsburgh, PA

[3]Department of Bioengineering, University of Pittsburgh, Pittsburgh PA

[4]Pittsburgh Hearing Research Center, University of Pittsburgh, Pittsburgh, PA

[5]Center for the Neural Basis of Cognition, University of Pittsburgh, Pittsburgh, PA

[6]Center for Neuroscience, University of Pittsburgh, Pittsburgh, PA

[7]Department of Biomedicine, University of Basel, Basel, CH

! These authors contributed equally

[*]To whom correspondence should be addressed:

Ross S. Williamson, PhD:

W1448 Biomedical Science Tower, 200 Lothrop Street, Pittsburgh, PA 15213

Email: rsw@pitt.edu

Thanos Tzounopoulos, PhD:

3017 Biomedical Science Tower 3, 3501 Fifth Avenue, Pittsburgh, PA 15261

Email: thanos@pitt.edu

Abstract

Peripheral trauma, such as noise-induced hearing loss (NIHL), triggers compensatory plasticity in the auditory cortex (ACtx) to maintain auditory function. While cortical plasticity in superficial cortical layers has been relatively well studied, the plasticity mechanisms governing deep-layer excitatory projection neurons remain less understood. Here, we investigated the plasticity of layer (L)5 extratelencephalic (ETs) and L6 corticothalamic neurons (CTs) following NIHL. Using a combination of *in vitro* slice electrophysiology, optogenetics, and *in vivo* two-photon imaging in a mouse model of NIHL, we characterized changes in evoked thalamocortical (TC) synaptic input strength, intrinsic excitability, and sound response properties. We found that TC input was initially equivalent between ETs and CTs, then shifted to CT-dominant one day after noise exposure. This shift renormalized to equivalent seven days after noise exposure and was associated with a transient increase in both the quantal size (q) in TC→CT synapses and intrinsic CT suprathreshold excitability. ETs maintained stable intrinsic properties and showed minor changes in their TC input. *In vivo* imaging revealed that CTs displayed a persistent elevation in sound intensity thresholds, whereas ETs transiently shifted their best frequency representation and reduced their responsiveness to high-frequency tones one day after NIHL, followed by recovery at seven days. Together, our findings highlight cell-type-specific plasticity mechanisms in deep-layer cortical neurons, enhance our understanding of cortical adaptation to peripheral damage, and highlight targets for developing therapeutic strategies to mitigate hearing loss and related disorders such as tinnitus and hyperacusis.

Short Abstract

Peripheral damage drives auditory cortex (ACtx) plasticity, but the underlying synaptic and cellular mechanisms remain poorly understood. We used a combination of *in vitro* slice electrophysiology, optogenetics, and *in vivo* two-photon imaging to investigate layer 5 extratelencephalic (ET) and layer 6 corticothalamic (CT) neuronal plasticity in mice, following noise-induced hearing loss (NIHL). Thalamocortical (TC) input was initially balanced between CTs and ETs but shifted to CT-dominant one day post-NIHL and then normalized by day seven. This transient shift was accompanied by increased quantal size and suprathreshold excitability in CTs, with minimal changes in ETs. *In vivo*, CTs exhibited persistent elevation in sound intensity thresholds, while ETs showed a transient shift in frequency tuning and reduced high-frequency responsiveness that recovered within a week. These findings reveal distinct, cell-type-specific plasticity mechanisms in deep-layer ACtx neurons following peripheral damage and highlight potential targets for treating hearing loss-related disorders such as tinnitus and hyperacusis.

Keywords

auditory cortex, noise-induced hearing loss, plasticity, thalamocortical circuits, excitatory neurons, in vivo imaging, in vitro electrophysiology

Introduction

In all sensory systems, damage to peripheral organs induces compensatory plasticity mechanisms in the brain, which contributes to function preservation by increasing neural responsiveness to surviving sensory inputs. In the cortex, this homeostatic plasticity is characterized by increased central gain and has been well documented across sensory modalities (Rasmusson, 1982; Merzenich et al., 1983; Robertson and Irvine, 1989; Kaas et al., 1990; Gilbert and Wiesel, 1992). In the auditory system, exposure to loud noise induces cochlear damage that often leads to a reduction in auditory nerve input due to cochlear synaptopathy and the degeneration or death of both hair and spiral ganglion cells (Ryan and Bone, 1978; Liberman and Dodds, 1984; Kujawa and Liberman, 2009). Despite this peripheral damage, the sound-evoked activity of excitatory cortical principal neurons (PNs) is frequently restored, or even enhanced, within days of NIHL (Qiu et al., 2000; Auerbach et al., 2014; Chambers et al., 2016; Resnik and Polley, 2017; Kumar et al., 2023), reflecting robust cortical and subcortical homeostatic plasticity mechanisms. These mechanisms support perceptual hearing threshold recovery, especially in quiet backgrounds, even after a dramatic loss of peripheral input (Chambers et al., 2016; Resnik and Polley, 2021)

In the ACtx, noise-induced cochlear damage is associated with enhanced central gain, reduced cortical inhibitory (GABAergic) activity, increased spontaneous firing, and reorganization of frequency tuning towards less damaged regions of the cochlea (Seki and Eggermont, 2003; Kotak et al., 2005; Sarro et al., 2008; Scholl and Wehr, 2008; Yang et al., 2011; Takesian et al., 2013; Chambers et al., 2016; Resnik and Polley, 2017). Recent studies in ACtx layer (L) 2/3 neurons revealed that this plasticity is mediated by cell-type-specific mechanisms enabling a precise division of labor and cooperativity amongst cortical interneurons (Kumar et al., 2023). However, the plasticity mechanisms governing excitatory projection neurons remain less understood. Addressing this knowledge gap requires examining the distinct contributions of deep-layer

90 neurons, specifically L5 extratelencephalic neurons (ETs, also known as pyramidal tract or PT
91 neurons) and L6 corticothalamic neurons (CTs), as L5 and 6 represent the primary output
92 pathways from the ACtx. CTs exclusively target the thalamus and readily modulate local cortical
93 gain, while also modulating ongoing thalamocortical oscillatory activity, forming key nodes in
94 cortico-thalamo-cortical loops (Olsen et al., 2012; Guo et al., 2017; Ibrahim et al., 2021; Shepherd
95 and Yamawaki, 2021). ETs, in addition to the thalamus, also project to the midbrain, striatum, and
96 amygdala (Harris and Shepherd, 2015; Chen et al., 2019; Williamson and Polley, 2019; Shepherd
97 and Yamawaki, 2021; Issa et al., 2023). These projections are crucial for connecting the auditory
98 system to downstream targets involved in motor control, sensorimotor integration, learning, and
99 higher-order cognitive processes (Winer, 2005; Bajo et al., 2010; Stebbings et al., 2014; Xiong et
100 al., 2015; Ford et al., 2024; Quass et al., 2024). It is therefore essential to determine how ETs,
101 CTs, as well as their thalamocortical inputs change after NIHL. Given the importance of cortico-
102 thalamo-cortical loops in perception and cognition in normal and pathological states (Tononi and
103 Edelman, 1998; Tononi et al., 1998; Jones, 2001; Llinas et al., 2005; Sherman, 2007; Shepherd
104 and Yamawaki, 2021), understanding these mechanisms may highlight novel approaches to
105 enhance perceptual recovery after hearing loss and/or mitigate plasticity-induced disorders such
106 as tinnitus and hyperacusis (Henton and Tzounopoulos, 2021).

107 To address these gaps in knowledge, we employed a mouse model of NIHL to investigate
108 plasticity mechanisms after noise trauma. We used a combination of *in vitro* slice
109 electrophysiology and *in vivo* two-photon imaging to characterize changes in thalamocortical
110 synaptic strength to ETs and CTs, and intrinsic and sound response properties of ETs and CTs
111 after NIHL. Our findings highlight cell-type-specific plasticity mechanisms, offering insights into
112 cortical plasticity in response to peripheral damage.
113
114

115 **Materials and Methods**

116 **Animals:** All mice handling was approved by the Institutional Animal Care and Use Committee at
117 the University of Pittsburgh. 66 male and 38 female Ntsr1-Cre mice (MMRRC, B6.FVB(Cg)-
118 Tg(Ntsr1-Cre)GN220Gsat/Mmcd), were used for experiments shown in Figures 1-5, S1-2; 7 male
119 and 2 female C57Bl/6J mice were used for Figure 6; 3 male and 1 female Ntsr1-Cre mice as well
120 as 4 male and 5 female Ntsr1-Cre x Ai148 mice (JAX, Ai148(TIT2L-GC6f-ICL-tTA2)-D) were used
121 for Figure 7.

122

123 **Surgical methods for *in vitro* electrophysiology:** Mice (P28-35) were anesthetized with
124 isoflurane (induction: 3% in oxygen, maintenance: 1.5-2% in oxygen) and secured in a stereotaxic
125 frame (Kopf). Core body temperature was maintained at ~37°C with a heating pad and eyes were
126 protected with ophthalmic ointment. Lidocaine (1%) was injected under the scalp and a midline
127 incision was made to expose the skull. ETs were retrogradely labeled by injecting green colored
128 fluorescent latex microspheres (Lumafluor) into the right inferior colliculus (1 mm posterior to
129 lambda and 1 mm lateral, at an injection depth of 0.75 mm), as schematized in **Figure 1A**. To
130 transduce CTs, an AAV (AAV9-FLEX-tdTomato, titer: $1e^{13}$ gc/mL; Addgene) was injected into the
131 right ACtx of Ntsr1-Cre mice through a small burr hole (~0.4 mm diameter, ~4 mm lateral to
132 lambda). A glass micropipette containing the viral vector was lowered into ACtx to a depth of ~1
133 mm using a micromanipulator (Kopf). A syringe pump (World Precision Instruments) was then
134 used to inject 200 nL (diluted 1:1 in PBS) over the course of 2 minutes, at a rate of 100 nL/min.

135

136 To facilitate stimulation of thalamic afferents, 500 nL (undiluted) of AAV9-CaMKIIa-
137 hChR2(H134R)-EYFP (titer: $8.96e^{13}$ gc/ml, Addgene) was injected into the right medial geniculate
138 body of Ntsr1-Cre mice (3 mm posterior/2 mm lateral/3mm depth) at a rate of 100 nL/min,
139 alongside injections of microspheres and AAV-FLEX-tdTomato, as described earlier. Post

140 injection, the scalp was closed with cyanoacrylate adhesive and mice were administered with a
141 subcutaneous injection of carprofen (5 mg/kg).
142
143 **Surgical methods for *in vivo* two-photon imaging:** Mice (P56-72) were anesthetized with
144 isoflurane (induction: 5% in oxygen, maintenance: 1.5-2% in oxygen) and secured in a stereotaxic
145 frame (Kopf). Dexamethasone (2 mg/kg) was administered via an intraperitoneal injection to
146 mitigate brain edema. Core body temperature was maintained at ~37°C with a heating pad and
147 eyes were protected with ophthalmic ointment. Lidocaine (1%) was injected under the scalp and
148 a midline incision was made to expose the skull. To transduce ETs, an AAV (AAVretro-hSyn1-
149 GCaMP6s-P2A-nls-tdTomato, titer: $5e^{12}$ gc/mL, Addgene), was injected into the right inferior
150 colliculus of C57 mice through a small burr hole (5 mm posterior to bregma and 1.2 mm lateral).
151 A glass micropipette containing the viral vector was lowered to depths of 0.3 and 0.8 mm using a
152 micromanipulator (Kopf). A syringe pump (Nanoject III, Drummond) was used to inject 300 nL at
153 each site at a rate of 10-15 nL/min. CTs were transduced with GCaMP6s through intracranial
154 injection into the ACtx (AAV5-Syn-FLEX.GCaMP6s.WPRE.SV40, titer: $7e^{12}$ gc/mL, Addgene) or
155 through transgenic crossing with the Ai148 mouse line. Post injection, the scalp was closed with
156 nylon sutures and mice were administered with a subcutaneous injection of carprofen (5 mg/kg).
157 Viruses were allowed to express for a minimum of three weeks prior to two-photon imaging.
158 Cranial windows were created by stacking three round glass coverslips (one 4 mm, two 3 mm, #1
159 thickness, Warner Instruments), etched with piranha solution (sulfuric acid and hydrogen
160 peroxide), then glued together with optically transparent, UV-cured adhesive (Norland Products,
161 Warner Instruments). The skull was exposed by removing the dorsal portion of the scalp and
162 periosteum and treated with etchant (C&B metabond) followed by 70% ethanol. A custom
163 stainless steel headplate (iMaterialize, (Romero et al., 2020)) was then attached to the skull using
164 dental cement (C&B metabond). A 3 mm circular craniotomy was made over right ACtx and the
165 cranial window was placed in the craniotomy. An airtight seal was achieved using Kwik-Sil (World

166 Precision Instruments) around the edge of the window prior to cementing into place. Vetbond (3M)
167 was used to bind the surrounding tissue to the dental cement. Following the implant surgery, mice
168 were administered with a subcutaneous injection of carprofen (5 mg/kg). Implants were allowed
169 to heal for at least five days before the first day of imaging.
170
171 **Slice electrophysiology:** Mice (P58-65) were first anesthetized with isoflurane and then
172 immediately decapitated. Brains were rapidly removed and coronal slices (300 μm) containing the
173 right ACtx were prepared in a cutting solution at 1 ^{o}C using a Vibratome (VT1200 S; Leica). The
174 cutting solution, pH 7.4, ~300 mOsm, contained the following (in mM): 2.5 KCl, 1.25 NaH_2PO_4,
175 25 $NaHCO_3$, 0.5 $CaCl_2$, 7 $MgCl_2$, 7 Glucose, 205 sucrose, 1.3 ascorbic acid, and 3 sodium
176 pyruvate (bubbled with 95% O_2/5% CO_2). The slices were immediately transferred and incubated
177 at 34°C in a holding chamber for 40 min before recording. The holding chamber contained ACSF,
178 containing the following (in mM): 125 NaCl, 2.5 KCl, 26.25 $NaHCO_3$, 2 $CaCl_2$, 1 $MgCl_2$, 10 glucose,
179 1.3 ascorbic acid, and 3 sodium pyruvate, pH 7.4, ~300 mOsm (bubbled with 95% O_2/5% CO_2).
180 Post incubation, the slices were stored at room temperature until the time of recording. Whole-
181 cell recordings in voltage- and current-clamp modes were performed on slices bathed in 31 ^{o}C
182 carbogenated ACSF, which was identical to the incubating solution. Borosilicate pipettes (World
183 Precision Instruments) were pulled into patch electrodes with 3–6 MΩ resistance (Sutter
184 Instruments) and filled with a potassium-based intracellular solution, which was used for whole-
185 cell current-clamp and contained (in mM): 128 K-gluconate, 10 HEPES, 4 $MgCl_2$, 4 Na_2ATP, 0.3
186 Tris-GTP, 10 Tris phosphocreatine, 1 EGTA, and 3 sodium ascorbate (pH = 7.25, 295 mOsm).
187 For recording thalamically evoked Excitatory Postsynaptic Currents (EPSCs), a cesium-based
188 internal solution containing (in mM): 126 $CsCH_3O_3S$, 4 $MgCl_2$ 10 HEPES, 4 Na_2ATP, 0.3 TrisGTP,
189 10 Tris-phosphocreatine, 1 CsEGTA, 1 QX-314, and 3 sodium ascorbate (pH = 7.25, 295 mOsm)
190 was used. For electrophysiological recordings, we used a MultiClamp-700B amplifier equipped
191 with Digidata-1440A A/D converter and Clampex (Molecular Devices). Data were sampled at 10

192 kHz and filtered at 4 kHz. Pipette capacitance was compensated and series resistance for
193 recordings was lower than 25 MΩ. Series resistance (R_{series}) was determined by giving a -5 mV
194 voltage step for 50 ms in voltage-clamp mode (command potential set at -70 mV) and was
195 monitored throughout the experiments. Recordings were excluded from further analysis if the
196 series resistance changed by more than 20% compared to the baseline period. R_{series} was
197 calculated by dividing the -5 mV voltage step by the peak current value generated immediately
198 after the step in the command potential. Input resistance (R_{input}) was calculated by giving a -5 mV
199 step in voltage-clamp mode (command potential set at -70 mV), which resulted in transient current
200 responses. The difference between baseline and steady-state hyperpolarized current (ΔI) was
201 used to calculate R_{input} using the following formula: R_{input} = -5 mV/ΔI - R_{series}. The average resting
202 membrane potential (V_{Rest}) was calculated by holding the neuron in voltage-follower mode (current
203 clamp, at I = 0) immediately after breaking in and averaging the membrane potential over the next
204 20 sec. In experiments used to study intrinsic properties of neurons, we added the following drugs:
205 20 μM DNQX (AMPA receptor antagonist), 50 μM APV (NMDA receptor antagonist), and 20 μM
206 SR 95531 Hydrobromide (Gabazine - a $GABA_A$ receptor antagonist). Depolarizing current pulses
207 (25 pA increments of 1-sec duration) in current clamp were injected to examine each neuron's
208 basic suprathreshold electrophysiological properties (baseline V_m was maintained at -70 mV, by
209 injecting the required current, if necessary). Action potential (AP) width was calculated as the full
210 width at the half-maximum amplitude of the first resulting action potential (AP) at rheobase. The
211 AP threshold was measured in phase plane as the membrane potential at which the
212 depolarization slope exhibited the first abrupt change (Δslope > 10 V/sec).
213
214 Light-evoked EPSCs and strontium quantal events (Sr^{2+}-mEPSCs) were evoked by optogenetic
215 stimulation of presynaptic axons. More specifically, a collimated blue LED light source (470 nm,
216 Thorlabs) was directed through a diaphragm and a 40x microscope objective lens and restricted
217 to a small spot in each stimulated cortical layer. Dual recordings targeted vertically aligned CT

218 and ET pairs. The light intensity that elicited a reliable stable plateau response, maximal
219 photostimulation, was determined on a cell pair basis with a short (0.15 ms duration) light pulse.
220 EPSCs were recorded in voltage clamp mode at -70 mV (peak values were averaged over a 1
221 ms time window) in the presence of sodium channel blocker tetrodotoxin (TTX, 1μM) to isolate
222 monosynaptic inputs and the potassium channel blocker 4-aminopyridine to depolarize the
223 terminals (4-AP, 100 μM). Representative traces for figures were acquired by averaging 10
224 consecutive EPSCs. Sr^{2+}-mEPSCs were recorded using a modified Sr^{2+}-ACSF solution, which
225 contained in mM: 125 NaCl, 2.5 KCl, 26 $NaHCO_3$, 4 $SrCl_2$, 4 $MgCl_2$, 15 glucose, 1.3 ascorbic acid,
226 and 3 sodium pyruvate, pH 7.4, ~300 mOsm, oxygenated w/ 95% O_2-5% CO_2. Slices were
227 incubated in this solution for 30 min prior to recording. All the other conditions were kept the same
228 as described earlier. The same cutting solution, Cs^+-based intracellular solution, and light
229 activation were used. Clampfit (11.2) was used for Sr^{2+}-mEPSCs analysis. A 400 ms window
230 before LED stimulation (pre-LED) and another 400 ms window starting 100 ms after LED onset
231 (post-LED) were analyzed. The amplitude of LED-evoked quantal events was calculated using
232 the following equation $\frac{[(Apost*Fpost)-(Apre*Fpre)]}{Fpost-Fpre}$, where $Apost$ is the average amplitude of post-
233 LED Sr^{2+}-mEPSCs, $Fpost$ is the average frequency of post-LED Sr^{2+}-mEPSCs, $Apre$ is the
234 average amplitude of pre-LED events, and $Fpre$ is the average frequency of pre-LED events
235 (Whitt et al., 2022). Event detection was optimized by pre-processing the traces with a lowpass
236 Gaussian filter (1kHz). Events (Sr^{2+}-mEPSCs) with rise time < 3 ms and amplitude > 3 root mean
237 square (RMS) were included. Cells with RMS noise > 2 or $Fpost$ - $Fpre$ < 2 Hz were excluded in
238 the analysis.
239

240 **Noise and sham exposure**

241 23-29 days after viral injections, mice (P50-55) were anesthetized with isoflurane (induction: 3%
242 in oxygen, maintenance: 1.5-2% in oxygen) during a unilateral exposure via insertion of a plastic

243 pipette tip into the left ear. The pipette tip was connected to a calibrated speaker (FT17H, Fostex,
244 Middleton, WI). Core body temperature was maintained at ~37°C with a heating pad and eyes
245 were protected with ophthalmic ointment. Sham- and noise-exposed mice were treated in the
246 same manner, but noise-exposed mice received 8-16 kHz octave broadband noise at 116 dB SPL
247 for one hour. A DS360 Ultra-Low Distortion Function Generator (Stanford Research Systems-
248 SRS) was used to generate bandwidth limiting using a 3-pole Butterworth filter. The speaker
249 (Type 4231, Bruel & Kjaer) was calibrated with a 1/4-inch microphone (4954-B, Bruel & Kjaer) to
250 accurately determine the voltage needed to generate the desired output.
251
252 **Auditory brainstem responses (ABRs)**
253 ABR measurements were made from the left (exposed) ear and conducted in a sound-attenuating
254 chamber (ENV-022SD; Med Associates). Subdermal electrodes were placed at the vertex
255 (active), ventral to the right pinna (ground), and ventral to the left pinna (reference), with a
256 calibrated speaker (CF-1; Tucker Davis Technologies) delivering acoustic stimuli to the left
257 (exposed) ear through a pipette tip fixed to a plastic tube connected to the speaker. ABR
258 measurements were obtained for tone bursts of 10, 16, 24, and 32 kHz in descending order from
259 80-0 dB SPL (or until 10 dB SPL below threshold). Threshold was defined as the lowest stimuli
260 intensity that produced a Wave 1 response. A Wave 1 response waveform was identified and
261 distinguished from non-response (noise) as the first consistent wave generated with decreased
262 amplitude and increased latency as intensity decreased. ABR measurements were collected
263 using BioSigRX software in response to 1 ms sound stimuli at a rate of 18.56 / sec, averaged
264 over 512 repetitions and filtered using a 300-3,000 Hz bandpass filter.
265
266 **Two-photon imaging**
267 At least three days prior to imaging, mice (P55-104) were acclimated to head fixation in the two-
268 photon rig for 30 minutes a day. Imaging was carried out at three timepoints: one day pre-

exposure (Day -1), one day post-exposure (Day 1), and seven days post-exposure (Day 7). ABRs were performed before each imaging session to measure peripheral sound responses. Mice with ABR click thresholds of 50 dB SPL or greater on Day -1 were excluded from the study. Noise-exposed mice were excluded if their click thresholds did not increase by at least 10 dB SPL from Day -1 to Day 1. Sham-exposed mice were excluded if their click thresholds exhibited an increase greater than 10 dB SPL from Day -1 to Day 1. On Day -1, widefield epifluorescence imaging was used to obtain a tonotopic map of ACtx to identify the location of primary area A1, as described previously (Romero et al., 2020). The two-photon field of view was then centered over A1 for all subsequent recordings. Two-photon excitation was delivered by an Insight X3 laser tuned to 940 nm (Spectra-Physics). A 16x/0.8NA water-immersion objective (Nikon) was used to obtain a 512 x 512 pixel field of view at 30 Hz with a Bergamo II Galvo-Resonant 8 kHz scanning microscope (Thorlabs). Scanning software (Thorlabs) and stimulus generation hardware (National Instruments) were synchronized with digital pulse trains. For both widefield and two-photon imaging, the microscope was rotated 40-55 degrees from the vertical axis to image the lateral portion of mouse ACtx while the mouse remained in an upright head position. Imaging was conducted in a dark, sound attenuating chamber and mice were monitored during experiments using infrared cameras (Genie Nano, Teledyne).

ETs were imaged 420-580 μm below the pial surface with a power of 45-130 mW. CTs were imaged 600-790 μm below the pial surface with a power of 111-150 mW. Fluorescence images were captured at either 1X (750 x 750 μm) or 2X (375 x 375 μm) digital zoom. Raw calcium videos were processed using Suite2P to accomplish motion correction, ROI detection, and spike deconvolution (Pachitariu M, 2016). All ROIs were visually validated, and any low quality or non-somatic ROIs were excluded. The same field of view was imaged at all three timepoints. Individual neurons were matched across days using ROIMatchPub, an open-source Matlab plugin (https://github.com/ransona/ROIMatchPub).

Each day of imaging included presentation of two stimulus sets. Eight pure tones (4 - 45 kHz in half-octave steps) were presented at four different intensities (20 - 80 dB SPL in 20 dB SPL steps). White noise bursts were presented at seven different intensities (20 - 80 dB SPL in 10 dB SPL steps). All stimuli were 50 ms in duration followed by a 2 s inter-trial interval. Stimuli were presented in pseudo-random order, and each stimulus was repeated 20 times.

Two-photon imaging analysis

Deconvolved calcium traces were normalized for each cell by z-scoring the trace relative to the average baseline activity (500 ms prior to sound onset). Evoked stimulus responses were quantified as the mean z-scored activity 0 - 500 ms following sound onset. To determine neural responsiveness for each stimulus, z-scored activity in this stimulus response period was compared to 1000 samples of randomly shifted responses (5 - 20 second shifts in the trace). A cell was deemed significantly responsive to a stimulus if the evoked stimulus response was greater than the 98th percentile of the randomly shifted dataset (adapted from Khoury et al 2023). The best frequency of each cell was determined as the frequency that elicited the largest z-scored response after averaging across intensity. Intensity thresholds were determined as the lowest intensity that evoked a significant z-scored response.

Stimulus decoding

We trained a multinomial logistic regression classifier to decode stimulus identity (either pure tone frequency at 80 dB SPL or white noise intensity) on a trial-by-trial basis. All neurons were pooled across mice for each exposure and day condition. Using 5-fold cross-validation, we trained the classifier with the mean evoked stimulus activity (0 - 500 ms following sound onset) of 200 randomly selected neurons. Decoding accuracy was quantified as the fraction of trials with correct stimulus classification in the held-out sample. Since our full dataset contained anywhere from 562

321 to 2687 neurons per group, we repeated this decoding strategy 2000 times, resampling (with
322 replacement) a new population of 200 neurons on every iteration, to generated a resampled
323 distribution of decoder accuracies for the population of neurons while ensuring decoding
324 accuracies were not biased by the number of neurons in each group. We then calculated the
325 mean and standard deviation of the decoder accuracy distribution in each exposure/day condition.
326 P values were computed explicitly from the bootstrapped distributions of decoding accuracies
327 (Day and Delgutte, 2016) .
328
329 **Image processing:** Image captioning in Figure 1C was achieved with Qcapture software. All
330 images were imported and processed using ImageJ (https://imagej.nih.gov/ij/).
331
332 **Statistics:** For statistical comparisons between two independent groups that passed the Shapiro-
333 Wilk normality test, we used unpaired t-tests. Mann-Whitney Rank-sum tests were used for non-
334 normally distributed data. For comparisons between multiple groups, we used N-way ANOVAs,
335 corrected for multiple comparisons. Significance levels are denoted as *$P < 0.05$, **$P < 0.01$,
336 ***$P < 0.001$, ****$P < 0.0001$. Group data are presented as mean ± SEM unless otherwise
337 specified. See tables for detailed values and statistical tests (Tables 1-2).
338
339
340 **Results**
341 To induce a stereotyped hearing loss, we followed standard approaches (Methods) and exposed
342 mice to 8-16 kHz octave broadband noise at 116 dB SPL for 1 hour (noise-exposed, NE). As a
343 control, we sham-exposed (SE) an additional cohort of littermate mice that underwent identical
344 procedures to NE but without the presence of noise. To assess hearing thresholds pre and post
345 noise- or sham-exposure (1-day and 7-day), we measured auditory brainstem responses (ABRs)
346 (**Figure S1A-C**), which reflect the synchronous activity of auditory nuclei in response to sound

347 arriving from the auditory nerve (wave I) to the inferior colliculus (wave V) (**Figure S1D**). We found
348 significantly elevated ABR thresholds and reduced wave I amplitudes in both one day (**Figure**
349 **S1A-D**) and 7 days after NE (**Figure S2A-C**) across all frequencies. ABR thresholds and wave I
350 amplitudes were not affected in SE mice (**Figure S1A-D**). Together, these data suggest that our
351 noise-exposure protocol results in threshold shifts that persist up to at least one week post NE.
352
353 **Transient shift in TC synaptic strength from CT and ET equivalent to CT dominant one day**
354 **after NE.**
355 Communication between the ACtx and the auditory thalamus, the medial geniculate body (MGB),
356 is mediated by reciprocally connected CT and TC pathways. TC neurons in the MGB strongly
357 innervate neurons in the ACtx, including ETs and CTs (Hooks et al., 2013; Yamawaki and
358 Shepherd, 2015). Yet, how NIHL affects TC synaptic strength onto ETs and CTs remains
359 unknown.
360
361 To address this question, we performed dual patch-clamp recordings by simultaneously patching
362 ETs and CTs from the same brain slice, while photoactivating TC axons. This recording
363 configuration allowed us to calculate the change in the ratio of the synaptic strength of TC→CT
364 over TC→ET synapses (CT/ET) in the same brain slice under identical experimental conditions.
365 Although it is not optimal to compare absolute EPSC amplitudes with optogenetically-induced
366 EPSC amplitudes, because of variable infection efficiency per mouse/brain area, we can
367 meaningfully apply this technique to detect noise-induced changes in the relative strength of
368 TC→CT vs. TC→ET synapses.
369
370 To study TC→CT and TC→ET synapses, we drove expression of channelrhodopsin (ChR2) in
371 CAMKII-expressing MGB neurons by injecting AAV-CaMKII-ChR2-YFP into the MGB (**Figure 1A-**

372 **C,** Methods). To stimulate ChR2-expressing TC axons, we used a collimated blue LED light
373 source, directed through a diaphragm and a 40x microscope objective lens. We recorded
374 monosynaptic photo-evoked AMPA receptor (AMPAR) EPSCs simultaneously from vertically
375 aligned ETs (green) and CTs (red) (**Figure 1 A-C**). To selectively label ETs (green) and identify
376 the boundaries of the ACtx, we injected green retrograde microspheres in the right inferior
377 colliculus (IC, **Figure 1A, and C middle**) (Joshi et al., 2015; Joshi et al., 2016). To selectively
378 label CTs (red), we injected Ntsr1-Cre transgenic mice, which selectively express Cre
379 recombinase in CTs, with the Cre-dependent AAV vector AAV-FLEX-tdTomato (**Figure 1C right**).
380 All electrophysiological experiments were performed in the presence TTX to block spikes, and 4-
381 AP to enhance presynaptic depolarization (see Methods). Because CT dendrites are primarily
382 limited to the deep cortical layers, we restricted our comparisons to L5-6 photostimulation (**Figure**
383 **1B**).
384
385 One day after noise exposure, we found a dramatic shift of the TC input from equivalent (ratio ~
386 1) to CT dominant (ratio > 5) (two-way ANOVA, main effect for exposure, $F = 5.44$, $p = 0.02$; main
387 effect for day, $F = 2.25$, $p = 0.14$). 7 days after NE, we observed a recovery of TC inputs to a
388 CT/ET equivalent state (**Figure 1D,E3-E4**). Together, these results suggest that noise exposure
389 leads to a dramatic change in auditory TC input favoring a greater thalamic excitation of CTs
390 compared to ETs one day after NIHL, which recovers seven days after trauma.
391
392 **Transient increase in the *q* on TC→CT synapses 1 day after NE**
393 To understand the underlying mechanisms of this shift towards greater relative thalamic excitation
394 in TC→CT compared to TC→ET synapses, we next investigated the synaptic properties of these
395 synapses and the intrinsic excitability of CTs and ETs after noise trauma. Because these
396 experiments were performed in TTX and 4-AP, and the ChR2 was activated to directly depolarize
397 terminals, the probability of release (p) is likely to be saturated at all synapses (n). We therefore

398 chose to assess the quantal size (*q*), first, in TC→CT synapses. To evaluate the amplitude of
399 quantal events, we replaced calcium (Ca^{2+}) with strontium (Sr^{2+}) in the bath solution (**Figure 2A-**
400 **D**). Sr^{2+} desynchronizes the evoked neurotransmitter release, thus allowing the analysis of
401 quantal events from the stimulated synapses (**Figure 2A-D**) (Oliet et al., 1996; Kouvaros et al.,
402 2020). In response to maximal photostimulation of L5-6, we found a significant increase in the
403 average amplitude of quantal events from the stimulated TC→CT synapses one day after NE
404 (unpaired t-test, p = 0.04; **Figure 2A-B**), which recovered 7 days after NE (unpaired t-test, p =
405 0.68; **Figure 2C-D**). This increase in *q* likely reflects an increase in TC→CT synaptic strength due
406 to either postsynaptic changes or changes in vesicle content. Consistent with these findings, we
407 found that the average L5-6 TC→CT EPSCs (average EPSCs elicited after L5-6 maximal
408 photostimulation) were significantly enhanced 1 day after NE compared to SE (Mann-Whitney
409 test, p = 0.004; **Figure 2E,F**), which then recovered 7 days after exposure (unpaired t-test, p =
410 0.94; **Figure 2G,H**). Together, these results suggest that the increase in *q* in TC→CT synapses
411 after noise trauma contributes to the greater relative thalamic excitation in TC→CT compared to
412 TC→ET after noise trauma.
413
414 **Transient increase in CT suprathreshold and transient increase in subthreshold intrinsic**
415 **excitability 1 day after NE**
416 Next, we investigated the effect of noise trauma on CT intrinsic excitability. Neither input
417 resistance (R_{input}) nor action potential width or threshold (AP_{width}, AP_{thres}) were affected either at 1
418 or 7 days after NE (**Figure 3A,C-D**). We found that the resting membrane potential (V_{rest}) was
419 more hyperpolarized 1 day after NE (two-way ANOVA, main effect for exposure, F = 19.81, p <
420 0.0001; main effect for day, F = 9.40, p = 0.003; exposure x day interaction, F = 6.91, p = 0.01;
421 **Figure 3B**). However, we found that the overall firing frequency in response to depolarization was
422 significantly increased 1 day after NE (two-way ANOVA, main effect for exposure, F = 9.45, p =

423 0.004; exposure x current steps interaction, F = 3.82, p < 0.0001; **Figure 3E-F**), suggesting an
424 increased suprathreshold excitability of CTs concurrent with the increased TC→CT input. There
425 were no differences in CT intrinsic excitability between SE and NE mice 7 days after exposure
426 (two-way ANOVA, main effect for exposure, F = 2.64, p = 0.11; exposure x current steps
427 interaction, F = 0.91, p = 0.52; **Figures 3G-H**). Taken together, these results suggest that
428 although there is a hyperpolarization on V_{rest} after NE, a combination of intrinsic and synaptic
429 mechanisms that increase TC→CT synaptic strength and CT suprathreshold excitability likely
430 contribute to the shift of TC input from equivalent between CT and ET to CT dominant one day
431 after noise exposure.
432
433 **No changes in the *q* of TC→ET synapses after NE**
434 We next assessed TC→ET synapses using a similar electrophysiological approach as in **Figure**
435 **2**. We found no changes in *q* either at 1 day or 7 days after exposure (1 day, Mann-Whitney test,
436 p = 0.64; 7 days, Mann-Whitney test, p > 0.9999; **Figure 4A-D**). Moreover, we found that the
437 average TC→ET EPSCs were significantly reduced one day after NE compared to SE (two-way
438 ANOVA, main effect for exposure, F = 8.32, p = 0.005; main effect for day, F = 0.05, p = 0.82;
439 exposure x day interaction, F = 4.97, p = 0.03; **Figure 4E-F_1**). This reduction was recovered 7
440 days after exposure (**Figure 4E,F_2**). Given that *p* is likely saturated in TC→ET synapses, and *q*
441 is unaltered, the reduction in L5-6 TC→ET EPSCs might be due to a decrease in *n*, or to the
442 previously mentioned limitations of this experimental setup in assessing changes in synaptic
443 strength, for changes in observed synaptic strength might be due to inconsistent degree of AAV
444 infection across animals (Discussion).
445
446 Because ETs have extensive dendrites throughout the cortical column, and TC projections to ETs
447 span several cortical layers (Harris and Shepherd, 2015; Ji et al., 2016), we also averaged

448 TC→ET EPSCs elicited after photostimulating L1-4 (L1-4 TC EPSCs) . No significant changes
449 were found at either 1 day or 7 days after NE (two-way ANOVA, main effect for exposure, F =
450 1.88, p = 0.18; main effect for day, F = 1.43, p = 0.24; exposure x day interaction, F = 3.35, p =
451 0.08; **Figure 4G-H**). Together, these results suggest that there is a cell-type-specific increase in
452 *q* in TC→CT synapses that likely contributes to the greater thalamic excitation of CTs compared
453 to ETs one day after NIHL.
454
455 **No changes in ET intrinsic excitability after NE**
456 After establishing that NIHL differentially affects TC onto ETs vs. CTs, we next investigated
457 whether noise exposure also alters the intrinsic excitability of these neurons in a cell-type-specific
458 manner. R_{input}, V_{rest}, AP_{width}, $AP_{threshold}$ and current-firing frequency function did not change either
459 at 1 day or 7 days post NE in ETs (**Figure 5A-H**). This finding supports cell-type-specific intrinsic
460 plasticity in deep layer neurons after NIHL, whereby ETs do not show plasticity while CTs show
461 a transient decrease in subthreshold excitability and a transient increase in suprathreshold
462 excitability. Together, these results suggest that the cell-type-specific increase in *q* in TC→CT
463 synapses and in suprathreshold CT intrinsic excitability likely contribute to the greater thalamic
464 excitation of CTs compared to ETs one day after NIHL.
465
466 **Changes in CT sound response properties persist 7 days after NE.**
467 To examine the consequences of NIHL in ET and CT sound response properties, we recorded
468 the sound-evoked activity of neural populations using two-photon (2P) calcium imaging. This
469 technique allowed us to longitudinally image the same populations of genetically defined cell-
470 types across time before and after noise exposure and characterize changes in sound response
471 properties. Head-fixed, awake mice passively listened to auditory stimuli, and we recorded
472 responses one day prior to exposure, then again one and seven days after exposure, matching

473 our previous electrophysiological studies. We selectively expressed GCaMP6s in CTs to examine
474 how CT responses to sounds change following NE (**Figure 6A**, see Methods). We imaged a total
475 of 4943 CTs across 8 unique fields of view in SE mice (-1d: 1649 neurons; 1d: 1681 neurons; 7d:
476 1613 neurons) and 7731 CTs across 14 unique fields of view in NE mice (-1d: 2687 neurons; 1d:
477 2546 neurons; 7d: 2498 neurons). We then determined which neurons were significantly active
478 during sound presentation and used these sound-responsive neurons for all subsequent analysis
479 (see Methods).
480
481 We first examined frequency responses by presenting pure tones of varying frequencies (4-45
482 kHz in 0.5 octave steps) and intensities (20-80 dB SPL in 20 dB SPL steps). Averaging across
483 intensity, we initially observed that CTs exhibited unstable frequency encoding, as evidenced by
484 fluctuations in average pure tone responses in SE animals (two-way ANOVA, main effect for day,
485 $F = 0.66$, $p = 0.52$; frequency × day interaction, $F = 3.68$, $p < 0.0001$; **Figure 6B**). Nevertheless,
486 we observed strong changes in CT sound responses following NE (two-way ANOVA, main effect
487 for day, $F = 11.62$, $p < 0.0001$; frequency × day interaction, $F = 2.78$, $p = 0.0004$; **Figure 6C**). CTs
488 exhibited increased population responses to low frequency sounds (4-11 kHz) 7 days after NE.
489 Next, we compared average population tuning curves by aligning activity to each neuron's best
490 frequency (BF) and comparing these aligned tuning curves across days. Frequency tuning curves
491 remained stable in SE mice (two-way ANOVA, main effect for day, $F = 0.52$, $p = 0.59$;
492 frequency × day interaction, $F = 0.81$, $p = 0.67$; **Figure 6D**). NE induced a slight but significant
493 increase in responses 0.5 octaves below BF (two-way ANOVA, main effect for day, $F = 9.36$, $p <$
494 0.0001; frequency × day interaction, $F = 0.52$, $p = 0.94$; **Figure 6E**). To investigate if individual
495 neurons altered their tuning preferences following noise exposure, we matched the same cells
496 across days and quantified changes in BF compared to baseline on day -1. While not significant,
497 CTs displayed a trend to decrease BF following NE (two-way ANOVA, main effect for exposure,
498 $F = 1.00$, $p = 0.32$; main effect for day, $F = 1.14$, $p = 0.32$; frequency × day interaction, $F = 1.33$,

499 $p = 0.27$; **Figure 6F**). To examine how these changes in frequency responses impacted
500 population encoding, we used a multinomial logistic regression model to predict stimulus
501 frequency from neural activity. Decoding frequency identity from CT activity did not reveal any
502 effect of noise exposure on population-level encoding (**Figure 6G**). Together, these results
503 suggest that noise exposure does not profoundly change CT frequency tuning.
504
505 We next examined intensity tuning by presenting broadband noise bursts between 20-80 dB SPL
506 (in 10 dB SPL steps). As with pure tone responses, CTs showed subtle changes in broadband
507 noise responses following SE (two-way ANOVA, main effect for day, $F = 3.54$, $p = 0.03$;
508 frequency × day interaction, $F = 2.51$, $p = 0.003$; **Figure 6H**). In contrast, there was a marked
509 decrease in intensity responses following NE (two-way ANOVA, main effect for day, $F = 13.87$, p
510 < 0.0001; frequency × day interaction term, $F = 5.45$, $p < 0.0001$; **Figure 6I**). Specifically, CTs
511 exhibited decreased activity in response to low intensity noise (< 60 dB SPL) following NE, which
512 did not recover by day 7. There was also a slight but significant increase in responses to 80 dB
513 SPL noise 7 days after NE. Consequently, NE led to a significant increase in intensity thresholds
514 (two-way ANOVA, main effect for exposure, $F = 14.75$, $p = 0.0002$; main effect for day, $F = 4.165$,
515 $p = 0.02$; frequency × day interaction, $F = 4.94$, $p = 0.008$; **Figure 6J**). Despite these changes,
516 decoding analyses did not reveal any significant changes in population encoding (**Figure 6K**).
517 Together, this suggests that noise exposure leads to decreased sensitivity in CTs to low intensity
518 noise that does not recover within a week.
519
520 **Transient changes in ET sound response properties 1 day after NE**
521 We next examined the activity of ETs through selective expression of GCaMP6s (**Figure 7A**, see
522 Methods). We imaged a total of 2337 ETs across 9 unique fields of view in SE mice (-1d: 705
523 neurons; 1d: 820 neurons; 7d: 812 neurons) and 1703 ET neurons across 8 unique fields of view

524 in NE mice (-1d: 562 neurons; 1d: 565 neurons; 7d: 576 neurons). As before, only neurons that
525 were significantly active during sound presentation were used for subsequent analyses.
526
527 We found that the average population responses to pure tones remained unchanged in SE mice
528 (two-way analysis of variance (ANOVA), main effect for day, $F = 0.68$, $p = 0.51$; frequency × day
529 interaction, $F = 1.03$, $p = 0.41$; **Figure 7B**). In contrast, NE led to a shift in the representation of
530 frequencies across the ET population (two-way ANOVA, main effect for day, $F = 19.35$,
531 $p < 0.0001$; frequency × day interaction, $F = 1.93$, $p = 0.02$; **Figure 7C**). One day after NE, the
532 average response to 23 kHz pure tones significantly decreased compared to baseline. This
533 reduction in activity then recovered to baseline levels by day 7 and was accompanied by a
534 significant increase in response to lower frequency sounds (11-16 kHz). BF-aligned tuning curves
535 were consistent across days in SE mice (two-way ANOVA, main effect for day, $F = 0.58$, $p = 0.56$;
536 frequency × day interaction, $F = 0.58$, $p = 0.90$; **Figure 7D**). Conversely, NE led to significant
537 changes in the average tuning curves (two-way ANOVA, main effect for day, $F = 12.03$,
538 $p < 0.0001$; frequency × day interaction, $F = 1.84$, $p = 0.02$; **Figure 7E**). Specifically, 7 days after
539 NE, ETs increased their responses at BF and one octave below BF (two-way ANOVA, main effect
540 for exposure, $F = 17.67$, $p < 0.0001$; main effect for day, $F = 2.23$, $p = 0.11$; exposure × day
541 interaction term, $F = 11.34$, $p < 0.0001$). This was accompanied by a significant decrease in BF
542 on day 1 which then recovered by day 7 in NE animals (**Figure 7F**). Frequency decoding revealed
543 that SE populations exhibited stable predictive accuracy across days, while NE led to a significant
544 decrease in accuracy on day 1 and a subsequent recovery on day 7 (**Figure 7G**). These findings
545 suggest that one day following NE, ETs reduce their activity at high frequencies and consequently
546 shift to lower BFs, decreasing the ability to accurately decode stimuli from population activity.
547 These perturbations then return to baseline seven days after NE.
548

549 We next examined whether ET intensity tuning changed following NE. As expected, noise
550 responses were similar across days in SE mice (two-way ANOVA, main effect for day, $F = 0.20$,
551 $p = 0.82$; intensity × day interaction, $F = 0.94$, $p = 0.50$; **Figure 7H**). We observed that NE led to
552 significant changes in intensity responses (two-way ANOVA, main effect for day, $F = 8.01$, $p =$
553 0.0003; frequency × day interaction term, $F = 2.90$, $p = 0.0005$; **Figure 7I**). One day after NE, ETs
554 displayed a loss of responses to low intensities (< 50 dB SPL) and a reduction in responses at
555 higher intensities. On day 7, responses partially recovered but remained below baseline for 70
556 dB SPL. We then quantified changes in single neuron intensity thresholds with cells matched
557 across imaging days (two-way ANOVA, main effect for exposure, $F = 11.23$, $p = 0.0009$; main
558 effect for day, $F = 6.56$, $p = 0.002$; exposure × day interaction, $F = 3.496$, $p = 0.03$; **Figure 7J**). One
559 day after NE, ETs displayed an increased threshold which reverted to baseline on day 7. We also
560 observed a threshold decrease on day 7 in SE mice. Finally, we decoded sound intensity from
561 population activity using multinomial logistic regression. Similar to our frequency decoding
562 findings, we found that decoding accuracy transiently decreased on day 1 following NE (**Figure**
563 **7K**). Together, these findings suggest that ETs recover from transient changes in tuning to both
564 frequency and intensity following noise exposure.
565

566 **Discussion**

567 Our findings provide new insights into the cellular and circuit mechanisms underlying the cortical
568 plasticity of deep-layer neurons in the auditory cortex (ACtx) following noise-induced hearing loss
569 (NIHL). We identified distinct changes in the synaptic, intrinsic, and sound response properties of
570 L5 ET and L6 CT neurons. These findings advance our understanding of ACtx plasticity after
571 peripheral damage and suggest a transient change in the relative strength of thalamocortical
572 inputs to ETs and CTs that may help maintain auditory function post-NIHL.
573

574 The observed changes in synaptic strength in thalamic input between ETs and CTs were
575 assessed using optogenetic approaches, which can be influenced by variability in viral infection
576 efficiency across animals and brain areas, and our recordings conditions where *p* is likely
577 saturated (**Figures 2E-H and 4E-H**). However, simultaneous recordings from ETs and CTs, which
578 mitigate these limitations, revealed a greater relative thalamic excitation of CTs compared to ETs
579 one day after NIHL (**Figure 1**). This finding, along with the increased *q* in TC→CT synapses
580 (**Figure 2A-D**) and the increased suprathreshold intrinsic CT excitability (**Figure 3E,F**), which are
581 independent of the variability in viral infection and *p* saturation, support an increase in
582 thalamocortical synaptic strength to CTs after noise trauma.
583
584 CTs form reciprocal and nonreciprocal feedback loops with the thalamus, modulating
585 thalamocortical activity through gain control and temporal filtering (Llano and Sherman, 2008;
586 Olsen et al., 2012; Mease et al., 2014; Guo et al., 2017; Clayton et al., 2021; Ibrahim et al., 2021).
587 We observed an overall increase in the intrinsic and synaptic excitability of CTs one day post-
588 NIHL, indicative of an enhanced overall CT excitability (**Figure 3F**). Since the corticothalamic
589 input from CTs to the non-lemniscal thalamic regions is also increased after noise trauma
590 (unpublished results from our lab currently in revision), and the non-lemniscal thalamic regions
591 are thought to be involved in higher-level processing related to internal state and prediction, this
592 increase may reflect a homeostatic plasticity mechanism aimed at enhancing perceptual recovery
593 after NIHL, likely via enhanced contextual modulation (Jones, 1998, 2001; Super et al., 2001;
594 Llinas et al., 2005; Larkum, 2013).
595
596 After NIHL, CTs exhibited a persistent reduction in responsiveness to low-intensity sounds
597 (**Figure 6H-K**), which cannot be explained by either increased thalamocortical input or intrinsic
598 excitability. Although the hyperpolarized V_{rest} observed 1 day after NE (**Figure 3B**) might
599 contribute, this is unlikely given that V_{rest} recovers 7 days after NE, but responsiveness to low-

intensity sounds does not. This suggests that the observed plasticity in response properties may involve changes in intracortical inputs. The reduction in low-intensity sound responsiveness may indicate long-term changes in the ability to detect quiet sounds, possibly reflecting a trade-off between sound detection and discrimination capabilities after NIHL, a function that has been prescribed to corticothalamic circuitry (Guo et al., 2017). This aligns with the role of CTs in modulating the temporal dynamics and gain of thalamocortical responses, potentially prioritizing detection of more reliable auditory signals.

In contrast to CTs, ETs did not show any changes in their intrinsic excitability after NIHL (**Figure 5**), consistent with previous studies (Nogueira et al., 2023). Although we did not observe any changes in *q* in TC→ET synapses (**Figure 4A-D**), which is the safest metric based on the limitations of our approach, we observed reduced thalamocortical input to ETs one day after noise exposure (**Figure 4E-F$_1$**), perhaps due to a decrease in *n* or to the limitations of our approach. However, this reduction is also consistent with the robust shift in the TC input from equivalent between CT and ET to CT dominant one day after NE.

When we explored the sound response properties of ETs, we observed a transient shift in their tuning properties following NIHL. Namely, one day after NE, ETs exhibited a reduction in responses to higher-frequency tones, accompanied by an increase in responsiveness to lower frequencies (**Figure 7**). This reduction in response is consistent with the hypothesized reduced TC input to ETs one day after NE (**Figure 4E-F$_1$**). The subsequent recovery of frequency tuning by seven days after NE is also consistent with the recovery of the lemniscal TC input to ETs (**Figure 4E,F$_2$**), and suggests that ACtx can dynamically recalibrate itself to restore normal auditory processing capabilities following transient disruptions.

625 Given our findings on the minimal plasticity changes in ETs after NIHL, the shift in responsiveness
626 of L5 ETs to lower frequencies is likely due to enhanced excitatory cortical inputs. This
627 hypothesized enhanced cortical input coincides with observed increased activity of the ET input
628 to the inferior colliculus after noise trauma (Asokan et al., 2018).
629
630 Our study complements and extends the demonstrated cell-type-specific plasticity among ACtx
631 L2/3 interneurons post NE (Kumar et al., 2023). This pattern of plasticity, characterized by
632 differential recovery of inhibitory neuron subtypes in L2/3, highlights the distinct adaptive
633 strategies employed across neurons and ACtx layers, whereby cell-type-specific plasticity in
634 superficial layers may prioritize gain control and network stability, whereas cell-type-specific
635 plasticity in deep layers may engage in adaptive mechanisms that preserve the balance between
636 detection/discrimination and higher-order processing functions (Guo et al., 2017). Although these
637 mechanisms are involved in homeostatic plasticity aimed to preserve hearing after cochlear
638 damage, the same mechanisms can also be involved in the generation of tinnitus and/or
639 hyperacusis, which are associated with noise-induced plasticity across all auditory brain centers,
640 including auditory cortex (Henton and Tzounopoulos, 2021).
641
642 In conclusion, our work reveals cell-type-specific plasticity in ACtx ETs and CTs following noise
643 trauma. The observed changes in synaptic strength, intrinsic properties, and sound response
644 tuning suggest a coordinated adaptive response aimed at preserving auditory function despite
645 significant peripheral damage. These findings contribute to a broader understanding of cortical
646 plasticity in sensory processing and may inform therapeutic strategies for mitigating the effects of
647 hearing loss and hearing loss-related disorders, such as tinnitus and hyperacusis.
648
649
650

Funding

This work was supported by NIH grants R01-DC019618 (TT), R01-DC020923 (TT), R21-DC018327 (RSW), R01-DC020459 (RSW), a Hearing Health Foundation Emerging Research Grant (RSW), and a Klingenstein-Simons Fellowship in Neuroscience (RSW).

Acknowledgements

We thank current and former members of the Tzounopoulos and Williamson Labs for helpful feedback and discussions, and assistance with animal care.

Author Contributions

Conceptualization: TT/RSW/SK

Supervision: TT/RSW

Methodology: YZ/SK/NAS/SL/MPA

Formal Analysis: YZ/SK/NAS/RFK

Writing – Original Draft: TT/RSW/SK

Writing – Review and Editing: YZ/SK/NAS/TT/RSW/MPA

672 **Figure Legends**

673

674 **Figure 1. Transient shift in TC synaptic strength from CT and ET equivalent to CT dominant**
675 **one day after NE.**

676 **(A)** Schematic illustration of stereotaxic injections of retrograde microspheres to label L5
677 extratelencephalic neurons (ETs, green), and viral vectors (AAVs) for expression of ChR2 in
678 thalamocortical (TC) inputs and tdTomato in L6 corticothalamic neurons (CTs, red) in Ntsr1-Cre
679 mice.

680 **(B)** Schematic illustration of slice electrophysiology experiment involving photostimulation of
681 ChR2 expressing TC afferents and simultaneous (dual) recording from an ET (green) and a CT
682 (red).

683 **(C)** Images in 4X magnification showing the extent of ACtx area in bright-field (left), green-labeled
684 ETs and TC axons (middle) and red-labeled CTs

685 **(D)** Average CT/ET EPSC ratio after optogenetically stimulating thalamic L5-6 input 1d and 7d
686 after SE and NE. (1d SE: 18 cells/6 mice; 1d NE: 26 cells/9 mice; 7d SE: 10 cells/6 mice; 7d NE:
687 10 cells/6 mice). Asterisks indicate significant differences (***$p<0.001$, two-way ANOVA and
688 Bonferroni correction for multiple comparisons).

689 **(E)** Representative traces of EPSCs in dual recordings from both CT (solid line) and ET (dotted
690 line) neurons evoked by maximal photostimulation of L5-6 thalamocortical inputs in 1d SE (E_1)
691 and 1d NE (E_2); 7d SE (E_3) and 7d NE (E_4). Different colored traces represent different pairs of
692 simultaneously recorded CTs and ETs.

693 Detailed statistical values are listed in Table 1.

694

695

696

697 **Figure 2. Transient increase in the *q* of TC→CT synapses 1 day after NE.**

698 **(A, C)** Average amplitude of light-evoked quantal EPSCs (Sr^{2+}-mEPSCs) in CTs in response to
699 L5-6 thalamocortical maximal photostimulation in 1d (A) and 7d (C), post SE (black) and NE (red)
700 mice (1d SE: 7 cells/3 mice; 1d NE: 6 cells/3 mice; 7d SE: 5 cells/2 mice; 7d NE: 6 cells/2 mice).
701 Asterisks indicate significant differences (*$p<0.05$, unpaired t-test).

702 **(B, D)** Representative Sr^{2+}-mEPSCs traces (top left) and representative average traces of quantal
703 Sr^{2+}-mEPSCs traces (top right). Amplitude histogram of events before (background noise) and
704 after stimulation from the same cell (bottom) in 1d (B) and 7d (D) after SE (black) and NE (red)
705 mice. The arrowhead indicates the onset of light stimulus. The dotted line indicates 400ms time
706 window before stimulus (pre-LED). The solid line represents a 400ms time window, which started
707 100 ms after the stimulus (post-LED) and was used to analyze the amplitude of Sr^{2+}-mEPSCs
708 (1d SE: 7 cells/3 mice; 1d NE: 6 cells/3 mice; 7d SE: 5 cells/2 mice; 7d NE: 6 cells/2 mice).

709 **(E, G)** Summary graph of the average CT EPSC amplitudes in response to L5-6 thalamocortical
710 maximal photostimulation in 1d (D) and 7d (F) SE (black) and NE (red). (1d SE: 18 cells/6 mice;
711 1d NE: 26 cells/9 mice; 7d SE: 10 cells/6 mice; 7d NE: 10 cells/6 mice). Asterisks indicate
712 significant differences (**$p<0.01$, Mann-Whitney test).

713 **(F, H)** Representative traces of L6 CT EPSCs in response to L5-6 thalamocortical maximal
714 photostimulation in 1d SE (E, black line) and 1d NE (E, red line) and 7d SE (G, black line) and 7d
715 NE (G, red line).

716 Detailed statistical values are listed in Table 1.

717

718

719 **Figure 3. Transient increase in suprathreshold CT intrinsic excitability 1 day after NE.**

720 **(A)** Average CT input resistance (R_{input}) 1d and 7d after SE (black) or NE (red) (1d SE: 22 cells/8

721 mice; 1d NE: 23 cells/5 mice; 7d SE: 23 cells/6 mice; 7d NE: 21 cells/4 mice).

722 **(B)** Average CT resting membrane potential (V_{rest}) 1d and 7d after SE (black) or NE (red) (1d SE:

723 22 cells/8 mice; 1d NE: 23 cells/5 mice; 7d SE: 23 cells/6 mice; 7d NE: 21 cells/4 mice).

724 **(C)** Average CT AP width 1d and 7d after SE (black) or NE (red) (1d SE: 21 cells/8 mice; 1d NE:

725 21 cells/5 mice; 7d SE: 23 cells/6 mice; 7d NE: 21 cells/4 mice).

726 **(D)** Average CT AP threshold of 1d and 7d after SE (black) or NE (red) (1d SE: 21 cells/8 mice;

727 1d NE: 19 cells/5 mice; 7d SE: 23 cells/6 mice; 7d NE: 21 cells/4 mice).

728 **(E_1, E_2, G_1, G_2)** Representative traces of CT firing in response to depolarizing current (50, 100,

729 200 pA current injections), 1d SE (E_1) vs. 1d NE (E_2); and 7d SE (G_1) vs. 7d NE (G_2).

730 **(F, H)** Average firing frequency as a function of injected current amplitude, 1d SE vs. 1d NE (F),

731 and 7d SE vs. 7d NE (H). Current injections from 25 to 250 pA with an increment of 25 pA (1d

732 SE: 21 cells/8 mice; 1d NE: 21 cells/5 mice; 7d SE: 23 cells/6 mice; 7d NE: 21 cells/4 mice).

733 Asterisks indicate significant differences (**$p<0.01$, two-way ANOVA and Bonferroni correction

734 for multiple comparisons).

735 Detailed statistical values are listed in Table 1.

736

737

738 **Figure 4. No changes in the *q* of TC→ET synapses after NE.**

739 **(A, C)** Average amplitude of Sr^{2+}-mEPSCs in ETs in response to L5-6 thalamocortical maximal
740 photostimulation in 1d (A) and 7d (B), post SE (black) and NE (red) (1d SE: 5 cells/4 mice; 1d NE:
741 7 cells/5 mice; 7d SE: 7 cells/2 mice; 7d NE: 5 cells/2 mice).

742 **(B, D)** Representative Sr^{2+}-mEPSCs traces (top left) and representative average traces of quantal
743 Sr^{2+}-mEPSCs traces (top right). Amplitude histogram of events before (background noise) and
744 after stimulation from the same cell (bottom) in 1d (B) and 7d (D) after SE (black) and NE (red)
745 mice. The arrowhead indicates the onset of light stimulus. The dotted line indicates 400ms time
746 window before stimulus (pre-LED). The solid line represents a 400ms time window, which started
747 100 ms after the stimulus (post-LED) and was used to analyze the amplitude of Sr^{2+}-mEPSCs (1d
748 SE: 5 cells/4 mice; 1d NE: 7 cells/5 mice; 7d SE: 7 cells/2 mice; 7d NE: 5 cells/2 mice).

749 **(E)** Representative traces of L5 ET EPSCs in response to L5-6 thalamocortical maximal
750 photostimulation in in 1d SE (E_1, black) vs. 1d NE (E_1, red), 7d SE (E_2, black) vs. 7d NE (E_2, red)
751 mice.

752 **(F)** Summary graph of the average L5 ET EPSC amplitudes in response to L1-4 thalamocortical
753 maximal photostimulation in 1d SE vs. 1d NE, or 7d SE vs. 7d NE mice (1d SE: 8 cells/3 mice; 1d
754 NE: 7 cells/4 mice; 7d SE: 9 cells/5 mice; 7d NE: 12 cells/4 mice).

755 **(G)** Representative traces of L5 ET EPSCs in response to L1-4 thalamocortical maximal
756 photostimulation in 1d SE (G_1, black) vs. 1d NE (G_1, red), 7d SE (G_2, black) vs 7d NE (G_2, red)
757 mice.

758 Detailed statistical values are listed in Table 1.

759

760

761 **Figure 5. No changes in ET intrinsic excitability after NE.**

762 **(A)** Average ET R_{input} 1d and 7d after SE (black) or NE (red) (1d SE: 21 cells/6 mice; 1d NE: 21
763 cells/5 mice; 7d SE: 20 cells/5 mice; 7d NE: 23 cells/6 mice).

764 **(B)** Average ET V_{rest} 1d and 7d after SE (black) or NE (red) (1d SE: 21 cells/6 mice; 1d NE: 21
765 cells/5 mice; 7d SE: 20 cells/5 mice; 7d NE: 23 cells/6 mice).

766 **(C)** Average ET AP width 1d and 7d after SE (black) or NE (red) (1d SE: 21 cells/6 mice; 1d NE:
767 21 cells/5 mice; 7d SE: 20 cells/5 mice; 7d NE: 23 cells/6 mice).

768 **(D)** Average ET AP threshold 1d and 7d after SE (black) or NE (red) (1d SE: 21 cells/6 mice; 1d
769 NE: 21 cells/5 mice; 7d SE: 20 cells/5 mice; 7d NE: 23 cells/6 mice).

770 **(E_1, E_2, G_1, G_2)** Representative traces of ET firing in response to depolarizing current injection
771 (50, 100, 200 pA), 1d SE (E_1) vs. 1d NE (E_2); and 7d SE (G_1) vs. 7d NE (G_2).

772 **(F, H)** Average firing frequency as a function of injected current amplitude, 1d SE vs. 1d NE (F),
773 and 7d SE vs. 7d NE (H). Current injections from 25 to 350 pA with an increment of 25 pA. (1d
774 SE: 21 cells/6 mice; 1d NE: 21 cells/5 mice; 7d SE: 20 cells/5 mice; 7d NE: 23 cells/6 mice).
775 Detailed statistical values are listed in Table 1.

776

777

Figure 6. Changes in CT sound response responses persist 7 days after NE.

(A) Example two-photon field of view from CTs imaged before and after exposure.

(B) Average responses to pure tones across all CTs in SE mice (-1d: n=507 neurons; 1d: n=460 neurons; 7d: n=432 neurons). Asterisks indicate significant pairwise differences.

(C) Same as (**A**) for NE mice (-1d: n=713 neurons; 1d: n=638 neurons; 7d: n=646 neurons). Asterisks indicate significant pairwise differences.

(D) Tuning curves aligned to best frequency (BF) in SE mice.

(E) Same as (**D**) for NE mice. Asterisks indicate significant pairwise differences (*$p<0.05$, Bonferroni corrected for multiple comparisons).

(F) Change in BF of matched cells in SE (black) and NE (red) mice (1d SE: n=40 neurons; 1d NE: n=36 neurons; 7d SE: n=35 neurons; 7d NE: n=40 neurons).

(G) Accuracy of a multinomial logistic regression classifier trained to decode the frequency of pure tones at 80 dB SPL. Dashed line represents chance level. Error bars represent standard deviation of decoding iterations.

(H) Average responses to white noise bursts at different intensities across all ETs in SE mice (-1d: n=438 neurons; 1d: n=460 neurons; 7d: n=411 neurons). Asterisks indicate significant pairwise differences (Bonferroni corrected for multiple comparisons).

(I) Same as (**H**) in NE mice (-1d: n=636 neurons; 1d: n=559 neurons; 7d: n=587 neurons). Asterisks indicate significant pairwise differences (Bonferroni corrected for multiple comparisons).

(J) Change in intensity thresholds across days in SE (black) and NE (red) mice (1d SE: n=27 neurons; 1d NE: n=31 neurons; 7d SE: n=29 neurons; 7d NE: n=25 neurons). Asterisks indicate significant pairwise differences (**$p<0.01$, ***$p<0.001$, Bonferroni corrected for multiple comparisons).

(K) Accuracy of a multinomial logistic regression trained to decode sound intensity. Dashed line represents chance level. Error bars represent standard deviation of decoding iterations.

Detailed statistical values are listed in Table 1.

Figure 7. Transient shift in ET sound response properties one day after NE.

(A) Example two-photon field of view from ETs imaged before and after exposure.

(B) Average responses to pure tones across all ETs in SE mice (-1d: n=385 neurons; 1d: n=414 neurons; 7d: n=400 neurons).

(C) Same as in (**A**) for NE mice (-1d: n=268 neurons; 1d: n=235 neurons; 7d: n=296 neurons). Asterisks indicate significant pairwise differences (Bonferroni corrected for multiple comparisons).

(D) Tuning curves aligned to best frequency (BF) in SE mice.

(E) Same as in (**D**) for NE mice. Asterisks indicate significant pairwise differences (*$p<0.05$, ****$p<0.0001$, Bonferroni corrected for multiple comparisons).

(F) Change in BF of matched cells in SE (black) and NE (red) mice (1d SE: n=68 neurons; 1d NE: n=54 neurons; 7d SE: n=68 neurons; 7d NE: n=71 neurons). Asterisks indicate significant pairwise differences (*$p<0.05$, ****$p<0.0001$, Bonferroni corrected for multiple comparisons).

(G) Accuracy of a multinomial logistic regression classifier trained to decode the frequency of pure tones at 80 dB SPL. Dashed line represents chance level. Error bars represent standard deviation of decoding iterations. Asterisks indicate significant pairwise differences (*$p<0.05$, ****$p<0.0001$, bootstrap test Bonferroni corrected for multiple comparisons).

(H) Average responses to white noise bursts at different intensities across all ETs in SE mice (-1d: n=331 neurons; 1d: n=270 neurons; 7d: n=299 neurons).

(I) Same as (**H**) in NE mice (-1d: n=226 neurons; 1d: n=222 neurons; 7d: n=252 neurons). Asterisks indicate significant pairwise differences (Bonferroni corrected for multiple comparisons).

(J) Change in intensity thresholds across days in SE (black) and NE (red) mice (1d SE: n=42 neurons; 1d NE: n=49 neurons; 7d SE: n=50 neurons; 7d NE: n=51 neurons). Asterisks indicate significant pairwise differences (*$p<0.05$, **$p<0.01$, Bonferroni corrected for multiple comparisons).

(K) Accuracy of a multinomial logistic regression trained to decode sound intensity. Dashed line represents chance level. Error bars represent standard deviation of decoding iterations. Asterisks

830 indicate significant pairwise differences (*$p<0.05$, bootstrap test Bonferroni corrected for multiple

831 comparisons).

832 Detailed statistical values are listed in Table 1.

833

834

835

836 **Figure S1. Changes in ABR threshold and Wave I amplitude 1 day after NE.**

837 **(A)** ABR threshold shifts 1d after SE and NE. For clicks and different tone frequencies, 1d SE:
838 24 mice; 1d NE: 25 mice; Asterisks indicate significant differences (****$p<0.0001$, clicks: Mann-
839 Whitney test; frequency: two-way ANOVA with Bonferroni correction for multiple comparison).

840 **(B)** ABR absolute thresholds for 1d NE (B1) and 1d SE (B2). For clicks and different tone
841 frequencies, -1d NE: 25 mice; 1d NE: 25 mice; -1dSE: 24 mice; 1d SE: 24 mice; Asterisks indicate
842 significant differences (****$p<0.0001$, clicks: Mann-Whitney test, frequency: two-way ANOVA with
843 Bonferroni correction for multiple comparison).

844 **(C)** Wave I amplitudes for -1d SE, 1d SE, -1d NE and 1d NE mice for clicks (C_1), 10 kHz (C_2), 16
845 kHz (C_3), 24 kHz (C_4) and 32 kHz (C_5). -1d SE: 14 mice; 1d SE: 14 mice; -1d NE: 14 mice; 1d NE:
846 14 mice. Detailed statistical values are listed in tables.

847 **(D)** Representative traces of ABR recordings (in response to 16 kHz tones) with thresholds
848 highlighted (dotted rectangle) before (left), 1d NE (middle), and 1d SE (right).
849 Detailed statistical values are listed in Table 2.

850

851

852 **Figure S2. Changes in ABR threshold and Wave I amplitude do not recover 7 days after**
853 **NE.**
854 **(A)** ABR threshold shifts 7d after SE and NE. For clicks and different tone frequencies, 7d SE: 12
855 mice; 7d NE: 13 mice; Asterisks indicate significant differences (**p<0.01, clicks, Mann-Whitney
856 test; ****p<0.0001, frequency, two-way ANOVA with Bonferroni correction for multiple
857 comparison).
858 **(B)** ABR absolute thresholds in 7d NE (B_1) and 7d SE (B_2). For clicks and frequency, -1d NE: 13
859 mice; 7d NE: 13 mice; -1d SE: 12 mice; 7d SE: 12 mice; Asterisks indicate significant differences
860 (***p<0.001, clicks, Mann-Whitney test; ****p<0.0001, frequency, mixed-effects with Bonferroni
861 correction for multiple comparison).
862 **(C)** Wave I amplitudes between -1d -SE, 7d SE, -1d -NE and 7d NE for clicks (C_1), 10 kHz (C_2),
863 16 kHz (C_3), 24 kHz (C_4) and 32 kHz (C_5). -1d -SE: 6 mice; 1d SE: 6 mice; -1d NE: 6 mice; 7d
864 NE: 6 mice.
865 Detailed statistical values are listed in Table 2.
866
867
868

References

Asokan MM, Williamson RS, Hancock KE, Polley DB (2018) Sensory overamplification in layer 5 auditory corticofugal projection neurons following cochlear nerve synaptic damage. Nat Commun 9:2468.

Auerbach BD, Rodrigues PV, Salvi RJ (2014) Central gain control in tinnitus and hyperacusis. Front Neurol 5:206.

Bajo VM, Nodal FR, Moore DR, King AJ (2010) The descending corticocollicular pathway mediates learning-induced auditory plasticity. Nat Neurosci 13:253-260.

Chambers AR, Resnik J, Yuan Y, Whitton JP, Edge AS, Liberman MC, Polley DB (2016) Central Gain Restores Auditory Processing following Near-Complete Cochlear Denervation. Neuron 89:867-879.

Chen X, Sun YC, Zhan H, Kebschull JM, Fischer S, Matho K, Huang ZJ, Gillis J, Zador AM (2019) High-Throughput Mapping of Long-Range Neuronal Projection Using In Situ Sequencing. Cell 179:772-786 e719.

Clayton KK, Williamson RS, Hancock KE, Tasaka GI, Mizrahi A, Hackett TA, Polley DB (2021) Auditory Corticothalamic Neurons Are Recruited by Motor Preparatory Inputs. Curr Biol 31:310-321 e315.

Day ML, Delgutte B (2016) Neural population encoding and decoding of sound source location across sound level in the rabbit inferior colliculus. J Neurophysiol 115:193-207.

Ford AN, Czarny JE, Rogalla MM, Quass GL, Apostolides PF (2024) Auditory Corticofugal Neurons Transmit Auditory and Non-auditory Information During Behavior. J Neurosci 44.

Gilbert CD, Wiesel TN (1992) Receptive field dynamics in adult primary visual cortex. Nature 356:150-152.

Guo W, Clause AR, Barth-Maron A, Polley DB (2017) A Corticothalamic Circuit for Dynamic Switching between Feature Detection and Discrimination. Neuron 95:180-194 e185.

Harris KD, Shepherd GM (2015) The neocortical circuit: themes and variations. Nat Neurosci 18:170-181.

Henton A, Tzounopoulos T (2021) What's the buzz? The neuroscience and the treatment of tinnitus. Physiol Rev 101:1609-1632.

Hooks BM, Mao T, Gutnisky DA, Yamawaki N, Svoboda K, Shepherd GM (2013) Organization of cortical and thalamic input to pyramidal neurons in mouse motor cortex. J Neurosci 33:748-760.

Ibrahim BA, Murphy CA, Yudintsev G, Shinagawa Y, Banks MI, Llano DA (2021) Corticothalamic gating of population auditory thalamocortical transmission in mouse. Elife 10.

Issa LK, Sekaran NVC, Llano DA (2023) Highly branched and complementary distributions of layer 5 and layer 6 auditory corticofugal axons in mouse. Cereb Cortex 33:9566-9582.

Ji XY, Zingg B, Mesik L, Xiao Z, Zhang LI, Tao HW (2016) Thalamocortical Innervation Pattern in Mouse Auditory and Visual Cortex: Laminar and Cell-Type Specificity. Cereb Cortex 26:2612-2625.

Jones EG (1998) Viewpoint: the core and matrix of thalamic organization. Neuroscience 85:331-345.

Jones EG (2001) The thalamic matrix and thalamocortical synchrony. Trends Neurosci 24:595-601.

Joshi A, Kalappa BI, Anderson CT, Tzounopoulos T (2016) Cell-Specific Cholinergic Modulation of Excitability of Layer 5B Principal Neurons in Mouse Auditory Cortex. J Neurosci 36:8487-8499.

Joshi A, Middleton JW, Anderson CT, Borges K, Suter BA, Shepherd GM, Tzounopoulos T (2015) Cell-specific activity-dependent fractionation of layer 2/3-->5B excitatory signaling in mouse auditory cortex. J Neurosci 35:3112-3123.

Kaas JH, Krubitzer LA, Chino YM, Langston AL, Polley EH, Blair N (1990) Reorganization of retinotopic cortical maps in adult mammals after lesions of the retina. Science 248:229-231.

Kotak VC, Fujisawa S, Lee FA, Karthikeyan O, Aoki C, Sanes DH (2005) Hearing loss raises excitability in the auditory cortex. J Neurosci 25:3908-3918.

Kouvaros S, Kumar M, Tzounopoulos T (2020) Synaptic Zinc Enhances Inhibition Mediated by Somatostatin, but not Parvalbumin, Cells in Mouse Auditory Cortex. Cereb Cortex 30:3895-3909.

Kujawa SG, Liberman MC (2009) Adding insult to injury: cochlear nerve degeneration after "temporary" noise-induced hearing loss. J Neurosci 29:14077-14085.

Kumar M, Handy G, Kouvaros S, Zhao Y, Brinson LL, Wei E, Bizup B, Doiron B, Tzounopoulos T (2023) Cell-type-specific plasticity of inhibitory interneurons in the rehabilitation of auditory cortex after peripheral damage. Nat Commun 14:4170.

Larkum M (2013) A cellular mechanism for cortical associations: an organizing principle for the cerebral cortex. Trends Neurosci 36:141-151.

Liberman MC, Dodds LW (1984) Single-neuron labeling and chronic cochlear pathology. III. Stereocilia damage and alterations of threshold tuning curves. Hear Res 16:55-74.

Llano DA, Sherman SM (2008) Evidence for nonreciprocal organization of the mouse auditory thalamocortical-corticothalamic projection systems. J Comp Neurol 507:1209-1227.

Llinas R, Urbano FJ, Leznik E, Ramirez RR, van Marle HJ (2005) Rhythmic and dysrhythmic thalamocortical dynamics: GABA systems and the edge effect. Trends Neurosci 28:325-333.

Mease RA, Krieger P, Groh A (2014) Cortical control of adaptation and sensory relay mode in the thalamus. Proc Natl Acad Sci U S A 111:6798-6803.

Merzenich MM, Kaas JH, Wall J, Nelson RJ, Sur M, Felleman D (1983) Topographic reorganization of somatosensory cortical areas 3b and 1 in adult monkeys following restricted deafferentation. Neuroscience 8:33-55.

Nogueira I, Lima TZ, Malfatti T, Leao KE (2023) Loud noise-exposure changes the firing frequency of subtypes of layer 5 pyramidal neurons and Martinotti cells in the mouse auditory cortex. Front Aging Neurosci 15:1152497.

Oliet SH, Malenka RC, Nicoll RA (1996) Bidirectional control of quantal size by synaptic activity in the hippocampus. Science 271:1294-1297.

Olsen SR, Bortone DS, Adesnik H, Scanziani M (2012) Gain control by layer six in cortical circuits of vision. Nature 483:47-52.

Pachitariu M SC, Dipoppa M, Schröder S, Rossi LF (2016) Suite2p : beyond 10 , 000 neurons with standard two-photon microscopy. bioRxiv:1-30.

Qiu C, Salvi R, Ding D, Burkard R (2000) Inner hair cell loss leads to enhanced response amplitudes in auditory cortex of unanesthetized chinchillas: evidence for increased system gain. Hear Res 139:153-171.

Quass GL, Rogalla MM, Ford AN, Apostolides PF (2024) Mixed Representations of Sound and Action in the Auditory Midbrain. J Neurosci 44.

Rasmusson DD (1982) Reorganization of raccoon somatosensory cortex following removal of the fifth digit. J Comp Neurol 205:313-326.

Resnik J, Polley DB (2017) Fast-spiking GABA circuit dynamics in the auditory cortex predict recovery of sensory processing following peripheral nerve damage. Elife 6.

Resnik J, Polley DB (2021) Cochlear neural degeneration disrupts hearing in background noise by increasing auditory cortex internal noise. Neuron.

Robertson D, Irvine DR (1989) Plasticity of frequency organization in auditory cortex of guinea pigs with partial unilateral deafness. J Comp Neurol 282:456-471.
Romero S, Hight AE, Clayton KK, Resnik J, Williamson RS, Hancock KE, Polley DB (2020) Cellular and Widefield Imaging of Sound Frequency Organization in Primary and Higher Order Fields of the Mouse Auditory Cortex. Cereb Cortex 30:1603-1622.
Ryan A, Bone RC (1978) Noise-induced threshold shift and cochlear pathology in the Mongolian gerbil. J Acoust Soc Am 63:1145-1151.
Sarro EC, Kotak VC, Sanes DH, Aoki C (2008) Hearing loss alters the subcellular distribution of presynaptic GAD and postsynaptic GABAA receptors in the auditory cortex. Cereb Cortex 18:2855-2867.
Scholl B, Wehr M (2008) Disruption of balanced cortical excitation and inhibition by acoustic trauma. J Neurophysiol 100:646-656.
Seki S, Eggermont JJ (2003) Changes in spontaneous firing rate and neural synchrony in cat primary auditory cortex after localized tone-induced hearing loss. Hear Res 180:28-38.
Shepherd GMG, Yamawaki N (2021) Untangling the cortico-thalamo-cortical loop: cellular pieces of a knotty circuit puzzle. Nat Rev Neurosci 22:389-406.
Sherman SM (2007) The thalamus is more than just a relay. Current Opinion in Neurobiology 17:417-422.
Stebbings KA, Lesicko AM, Llano DA (2014) The auditory corticocollicular system: molecular and circuit-level considerations. Hear Res 314:51-59.
Super H, Spekreijse H, Lamme VA (2001) Two distinct modes of sensory processing observed in monkey primary visual cortex (V1). Nat Neurosci 4:304-310.
Takesian AE, Kotak VC, Sharma N, Sanes DH (2013) Hearing loss differentially affects thalamic drive to two cortical interneuron subtypes. J Neurophysiol 110:999-1008.
Tononi G, Edelman GM (1998) Consciousness and complexity. Science 282:1846-1851.
Tononi G, Edelman GM, Sporns O (1998) Complexity and coherency: integrating information in the brain. Trends Cogn Sci 2:474-484.
Whitt JL, Ewall G, Chakraborty D, Adegbesan A, Lee R, Kanold PO, Lee HK (2022) Visual Deprivation Selectively Reduces Thalamic Reticular Nucleus-Mediated Inhibition of the Auditory Thalamus in Adults. J Neurosci 42:7921-7930.
Williamson RS, Polley DB (2019) Parallel pathways for sound processing and functional connectivity among layer 5 and 6 auditory corticofugal neurons. Elife 8.
Winer JA (2005) Decoding the auditory corticofugal systems. Hear Res 207:1-9.
Xiong XR, Liang F, Zingg B, Ji XY, Ibrahim LA, Tao HW, Zhang LI (2015) Auditory cortex controls sound-driven innate defense behaviour through corticofugal projections to inferior colliculus. Nat Commun 6:7224.
Yamawaki N, Shepherd GM (2015) Synaptic circuit organization of motor corticothalamic neurons. J Neurosci 35:2293-2307.
Yang S, Weiner BD, Zhang LS, Cho SJ, Bao S (2011) Homeostatic plasticity drives tinnitus perception in an animal model. Proc Natl Acad Sci U S A 108:14974-14979.

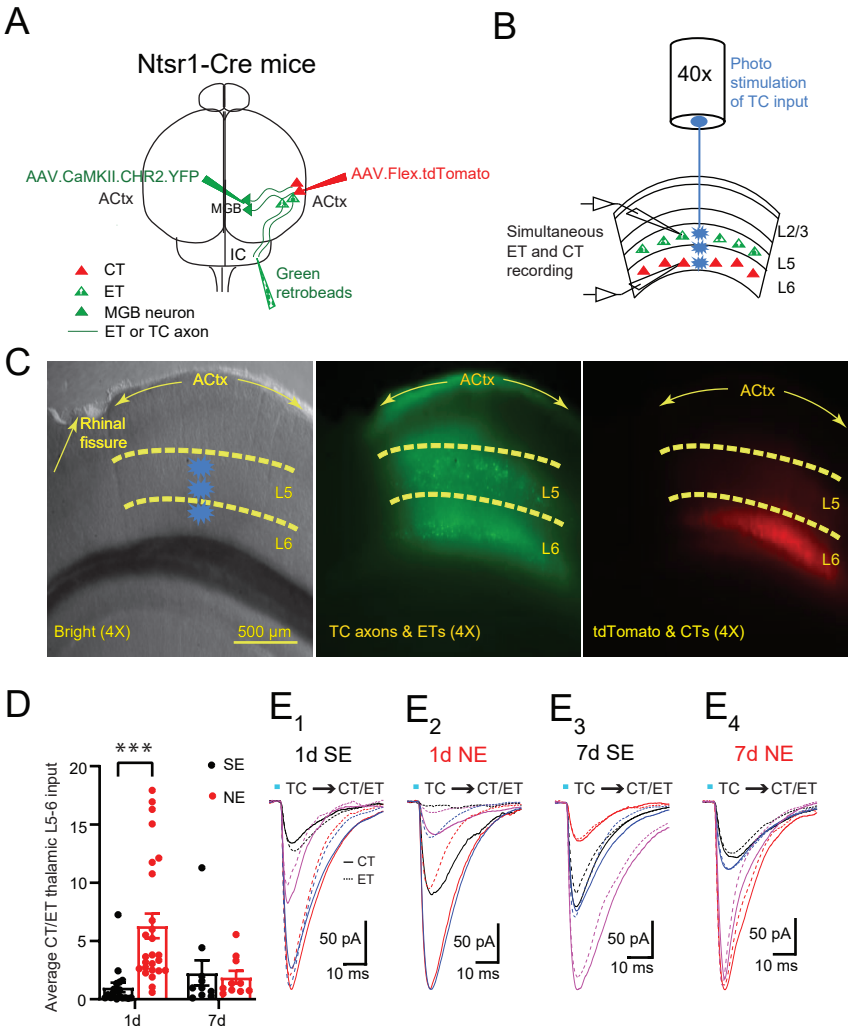
A
Ntsr1-Cre mice
AAV.CaMKII.CHR2.YFP
ACtx
MGB
IC
AAV.Flex.tdTomato
ACtx
Green retrobeads
CT
ET
MGB neuron
ET or TC axon
B
40x
Photo stimulation of TC input
Simultaneous ET and CT recording
L2/3
L5
L6
C
ACtx
Rhinal fissure
L5
L6
Bright (4X)
500 µm
TC axons & ETs (4X)
tdTomato & CTs (4X)
D
Average CT/ET thalamic L5-6 input
***
SE
NE
1d
7d
E1
1d SE
E2
1d NE
E3
7d SE
E4
7d NE
TC → CT/ET
CT
ET
50 pA
10 ms

Figure 1

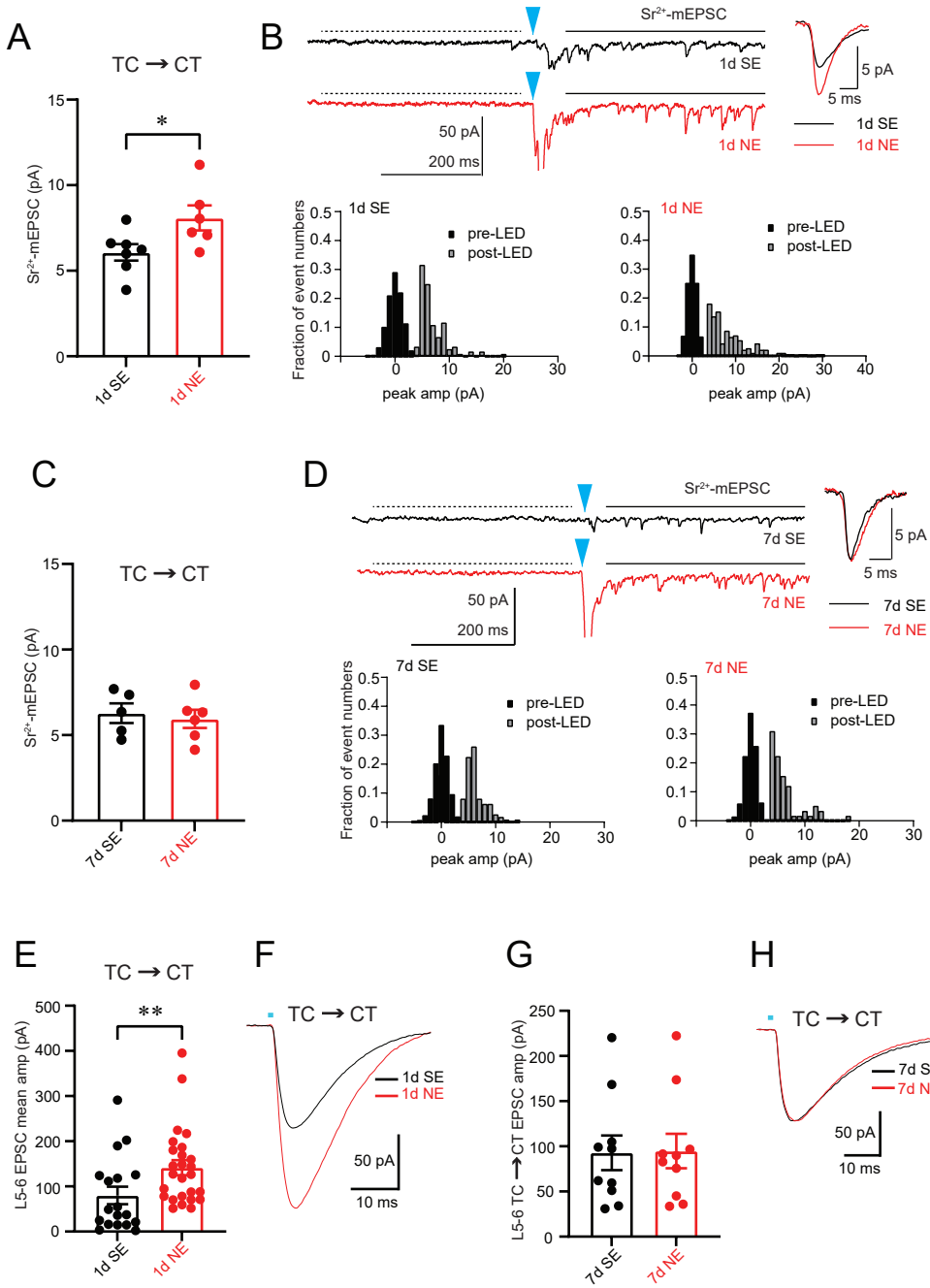
A
TC → CT
Sr²⁺-mEPSC (pA)
*
1d SE
1d NE
B
Sr²⁺-mEPSC
1d SE
1d NE
50 pA
200 ms
5 pA
5 ms
Fraction of event numbers
pre-LED
post-LED
peak amp (pA)
C
TC → CT
Sr²⁺-mEPSC (pA)
7d SE
7d NE
D
Sr²⁺-mEPSC
7d SE
7d NE
50 pA
200 ms
5 pA
5 ms
Fraction of event numbers
pre-LED
post-LED
peak amp (pA)
E
TC → CT
L5-6 EPSC mean amp (pA)
**
1d SE
1d NE
F
TC → CT
1d SE
1d NE
50 pA
10 ms
G
L5-6 TC → CT EPSC amp (pA)
7d SE
7d NE
H
TC → CT
7d SE
7d NE
50 pA
10 ms

Figure 2

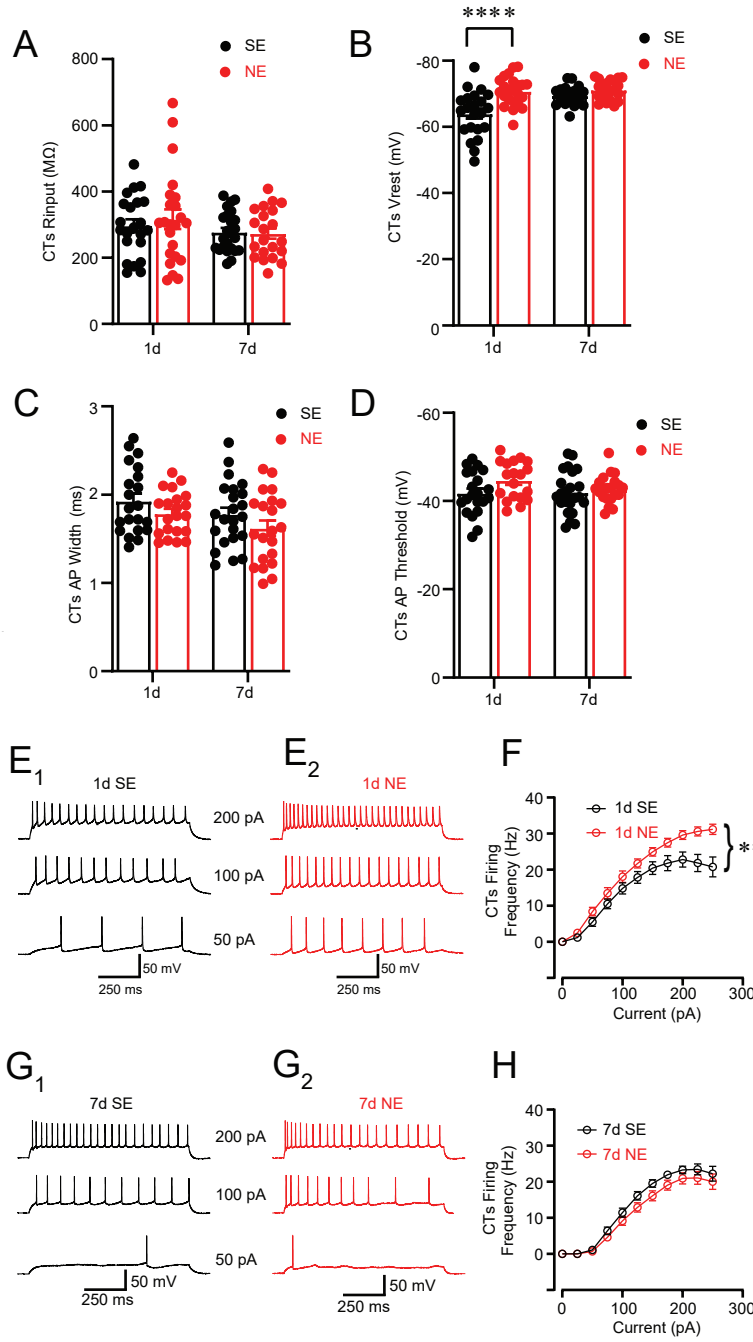
A
SE
NE
CTs Rinput (MΩ)
800
600
400
200
0
1d
7d
B
****
SE
NE
CTs Vrest (mV)
-80
-60
-40
-20
0
1d
7d
C
SE
NE
CTs AP Width (ms)
3
2
1
0
1d
7d
D
SE
NE
CTs AP Threshold (mV)
-60
-40
-20
0
1d
7d
E1
1d SE
200 pA
100 pA
50 pA
50 mV
250 ms
E2
1d NE
50 mV
250 ms
F
1d SE
1d NE
**
CTs Firing Frequency (Hz)
40
30
20
10
0
0
100
200
300
Current (pA)
G1
7d SE
200 pA
100 pA
50 pA
50 mV
250 ms
G2
7d NE
50 mV
250 ms
H
7d SE
7d NE
CTs Firing Frequency (Hz)
40
30
20
10
0
0
100
200
300
Current (pA)

Figure 3

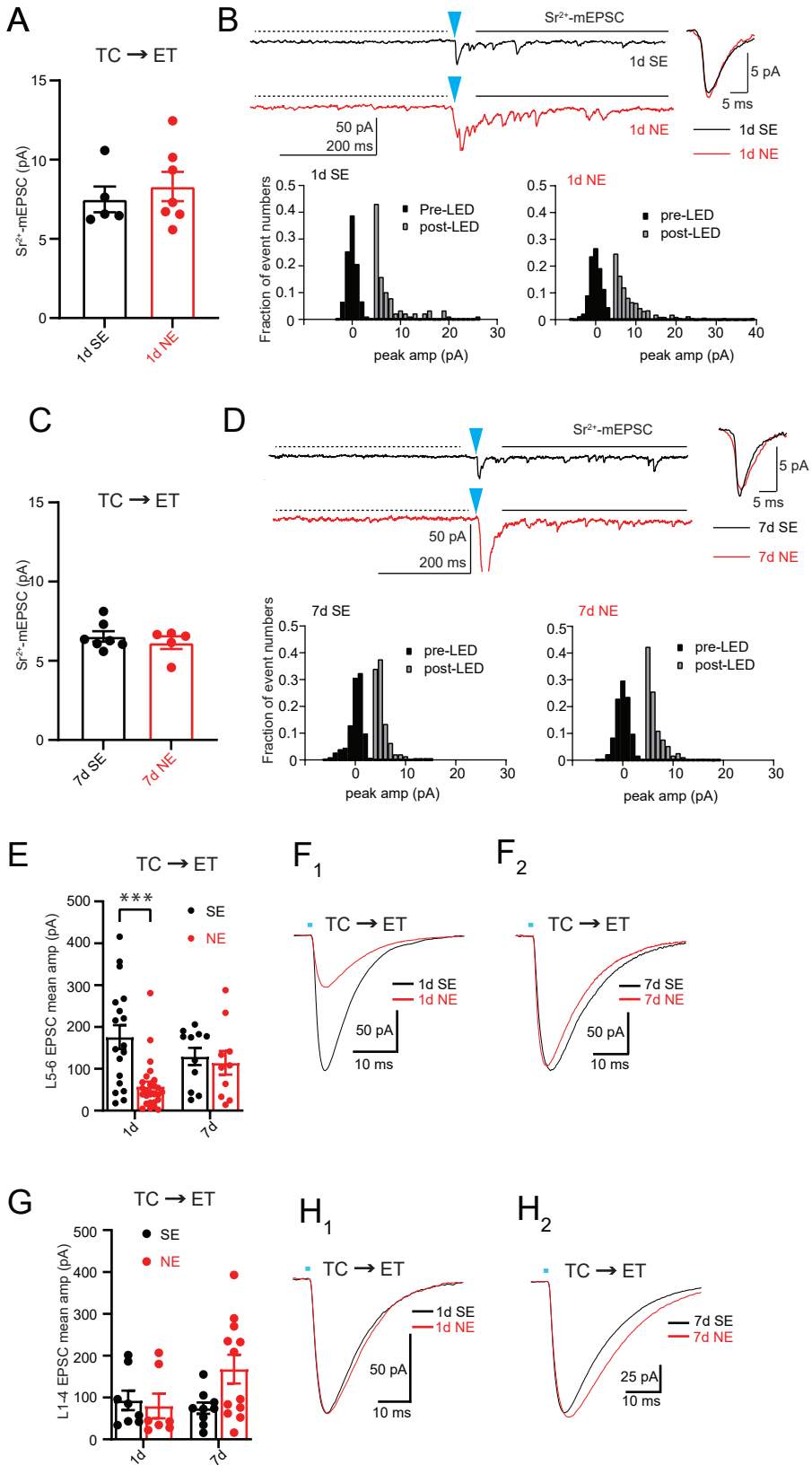
A
TC → ET
Sr2+-mEPSC (pA)
1d SE
1d NE
B
Sr2+-mEPSC
1d SE
1d NE
50 pA
200 ms
5 pA
5 ms
Fraction of event numbers
Pre-LED
post-LED
peak amp (pA)
C
7d SE
7d NE
D
E
L5-6 EPSC mean amp (pA)
SE
NE
1d
7d
F1
F2
G
L1-4 EPSC mean amp (pA)
H1
H2
25 pA
10 ms

Figure 4

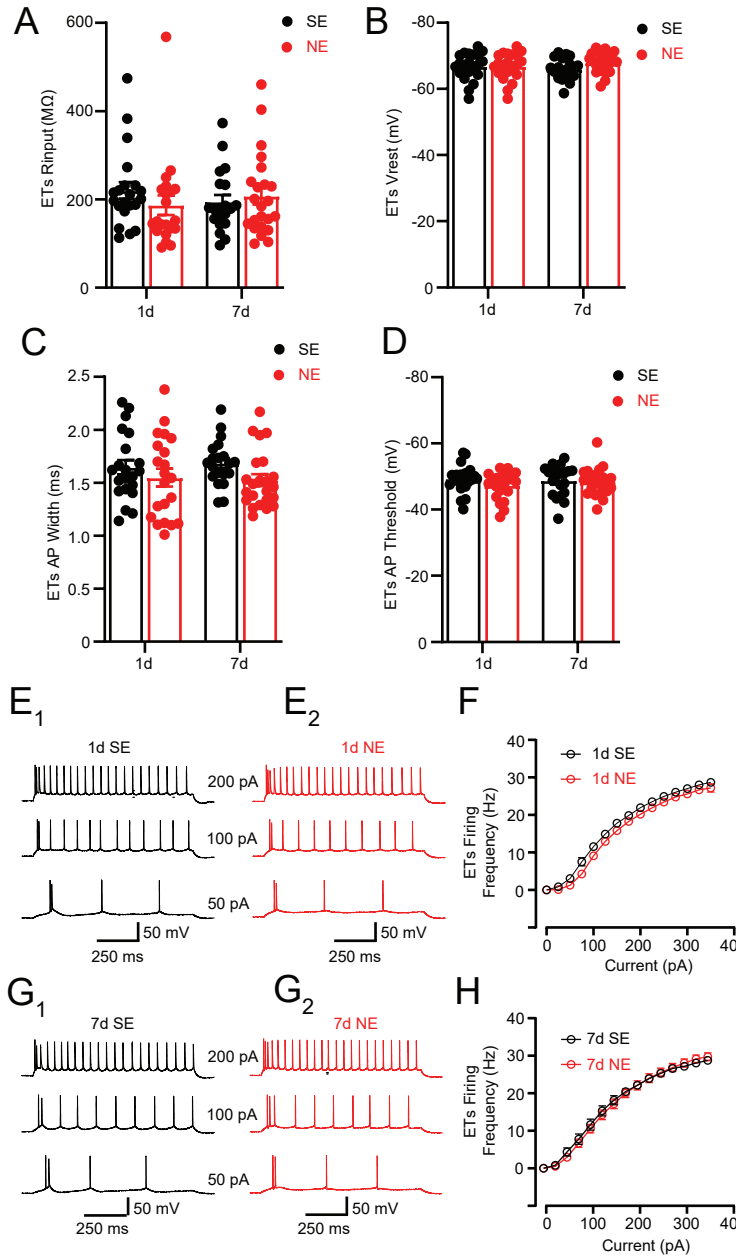
A
ETs Rinput (MΩ)
600
400
200
0
1d
7d
SE
NE
B
ETs Vrest (mV)
-80
-60
-40
-20
0
1d
7d
SE
NE
C
ETs AP Width (ms)
2.5
2.0
1.5
1.0
0.5
0
1d
7d
SE
NE
D
ETs AP Threshold (mV)
-80
-60
-40
-20
0
1d
7d
SE
NE
E1
1d SE
200 pA
100 pA
50 pA
50 mV
250 ms
E2
1d NE
200 pA
100 pA
50 pA
50 mV
250 ms
F
ETs Firing Frequency (Hz)
40
30
20
10
0
1d SE
1d NE
0
100
200
300
400
Current (pA)
G1
7d SE
200 pA
100 pA
50 pA
50 mV
250 ms
G2
7d NE
200 pA
100 pA
50 pA
50 mV
250 ms
H
ETs Firing Frequency (Hz)
40
30
20
10
0
7d SE
7d NE
0
100
200
300
400
Current (pA)

Figure 5

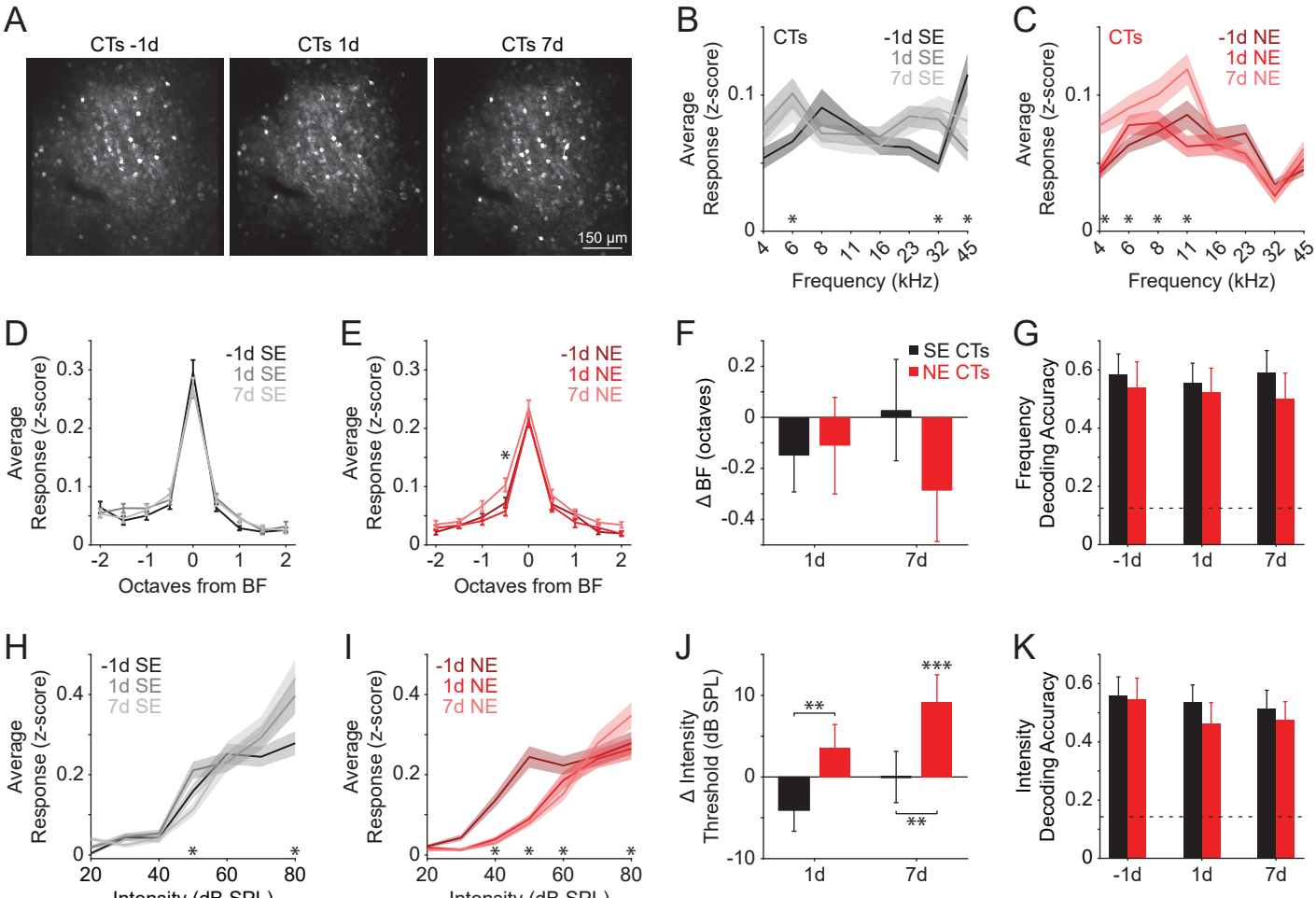
A
CTs -1d
CTs 1d
CTs 7d
150 µm
B
CTs
-1d SE
1d SE
7d SE
Average Response (z-score)
Frequency (kHz)
C
CTs
-1d NE
1d NE
7d NE
Average Response (z-score)
Frequency (kHz)
D
-1d SE
1d SE
7d SE
Average Response (z-score)
Octaves from BF
E
-1d NE
1d NE
7d NE
Average Response (z-score)
Octaves from BF
F
SE CTs
NE CTs
Δ BF (octaves)
1d
7d
G
Frequency Decoding Accuracy
-1d
1d
7d
H
-1d SE
1d SE
7d SE
Average Response (z-score)
Intensity (dB SPL)
I
-1d NE
1d NE
7d NE
Average Response (z-score)
Intensity (dB SPL)
J
Δ Intensity Threshold (dB SPL)
1d
7d
K
Intensity Decoding Accuracy
-1d
1d
7d

Figure 6

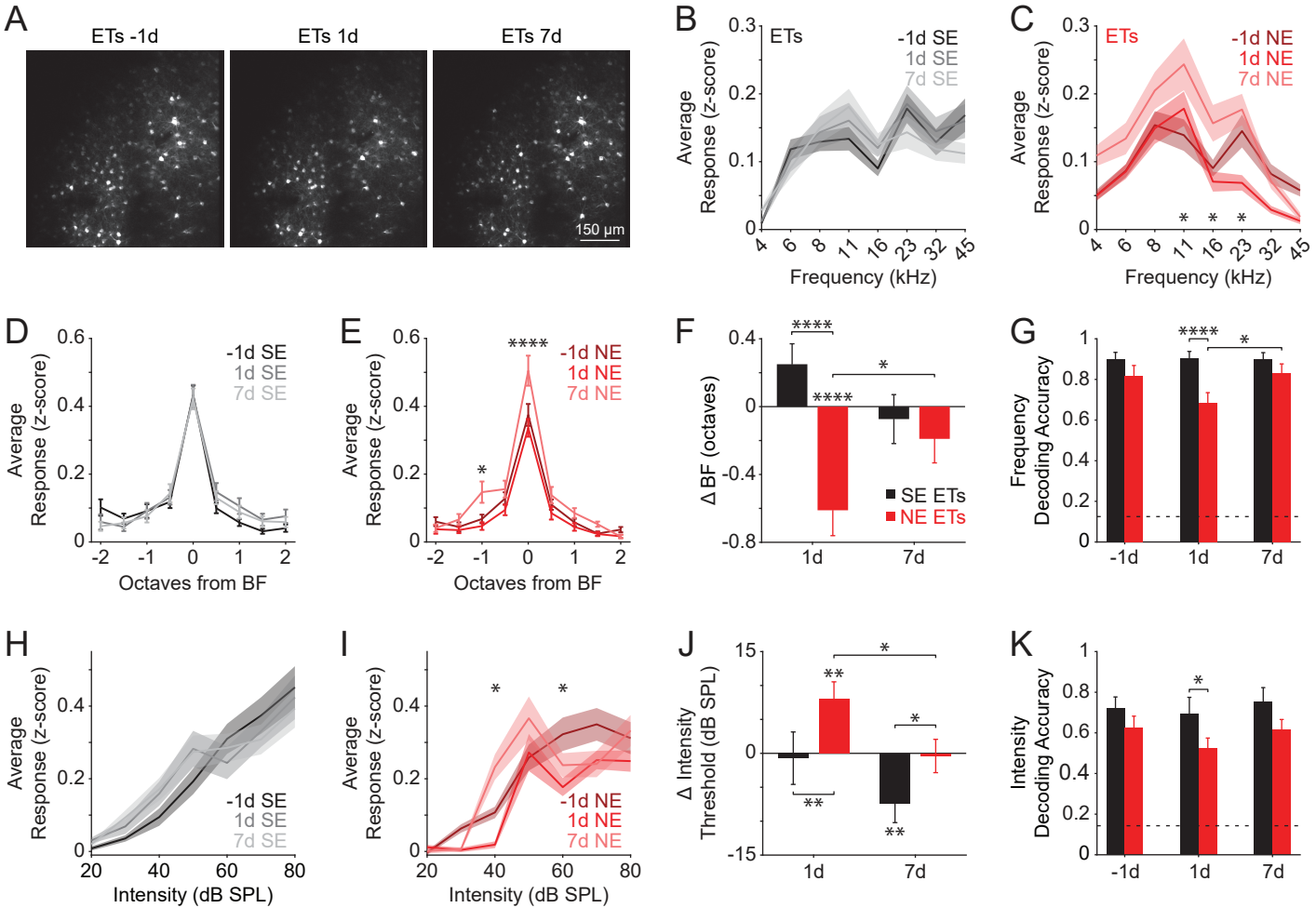
A
ETs -1d
ETs 1d
ETs 7d
150 µm
B
ETs
-1d SE
1d SE
7d SE
Average Response (z-score)
Frequency (kHz)
C
ETs
-1d NE
1d NE
7d NE
Average Response (z-score)
Frequency (kHz)
D
-1d SE
1d SE
7d SE
Average Response (z-score)
Octaves from BF
E
-1d NE
1d NE
7d NE
Average Response (z-score)
Octaves from BF
F
Δ BF (octaves)
SE ETs
NE ETs
1d
7d
G
Frequency Decoding Accuracy
-1d
1d
7d
H
-1d SE
1d SE
7d SE
Average Response (z-score)
Intensity (dB SPL)
I
-1d NE
1d NE
7d NE
Average Response (z-score)
Intensity (dB SPL)
J
Δ Intensity Threshold (dB SPL)
1d
7d
K
Intensity Decoding Accuracy
-1d
1d
7d

Figure 7

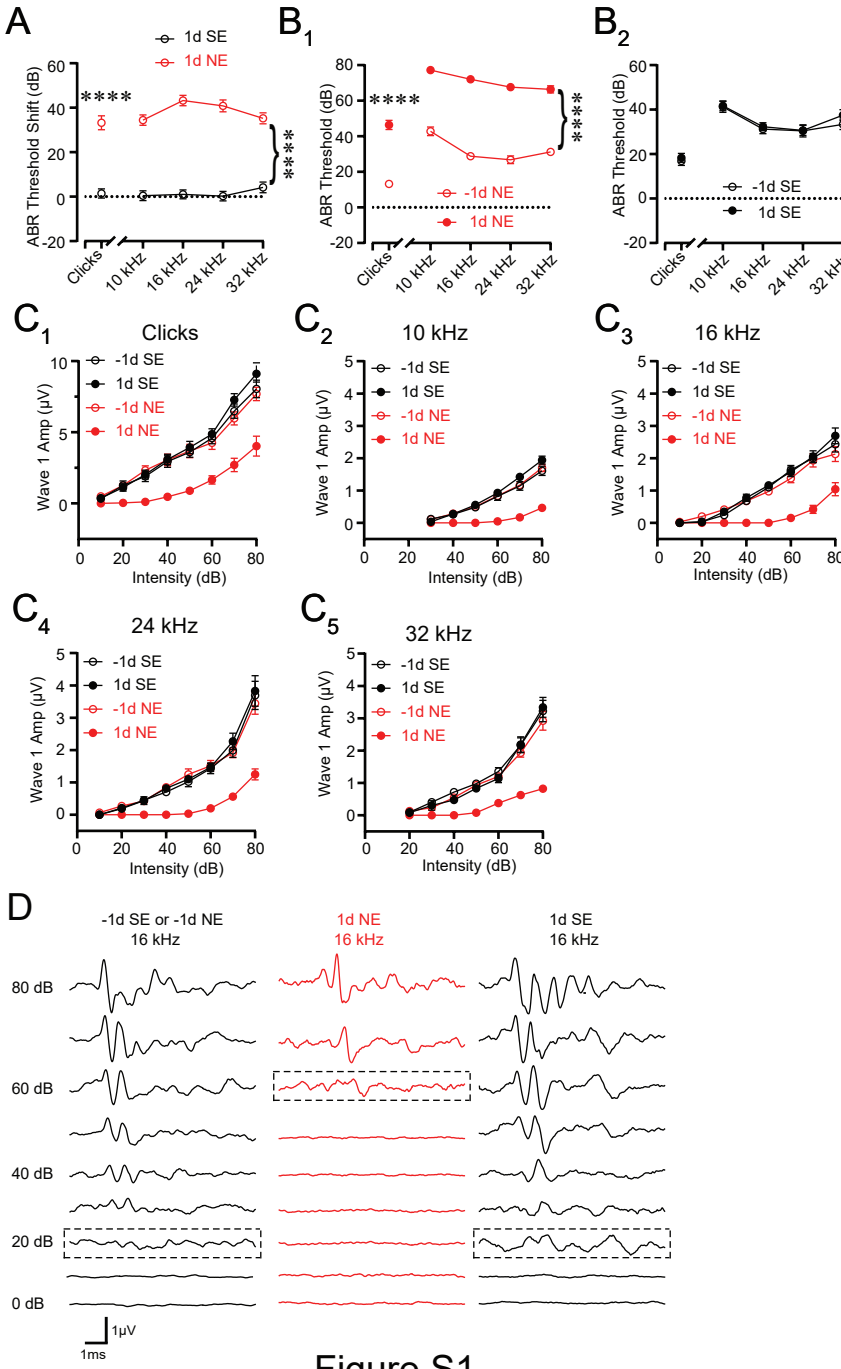
A
1d SE
1d NE
ABR Threshold Shift (dB)
****
****
Clicks
10 kHz
16 kHz
24 kHz
32 kHz
B1
ABR Threshold (dB)
-1d NE
1d NE
B2
-1d SE
1d SE
C1
Clicks
C2
10 kHz
C3
16 kHz
C4
24 kHz
C5
32 kHz
Wave 1 Amp (μV)
Intensity (dB)
D
-1d SE or -1d NE
16 kHz
1d NE
16 kHz
1d SE
16 kHz
80 dB
60 dB
40 dB
20 dB
0 dB
1μV
1ms

Figure S1

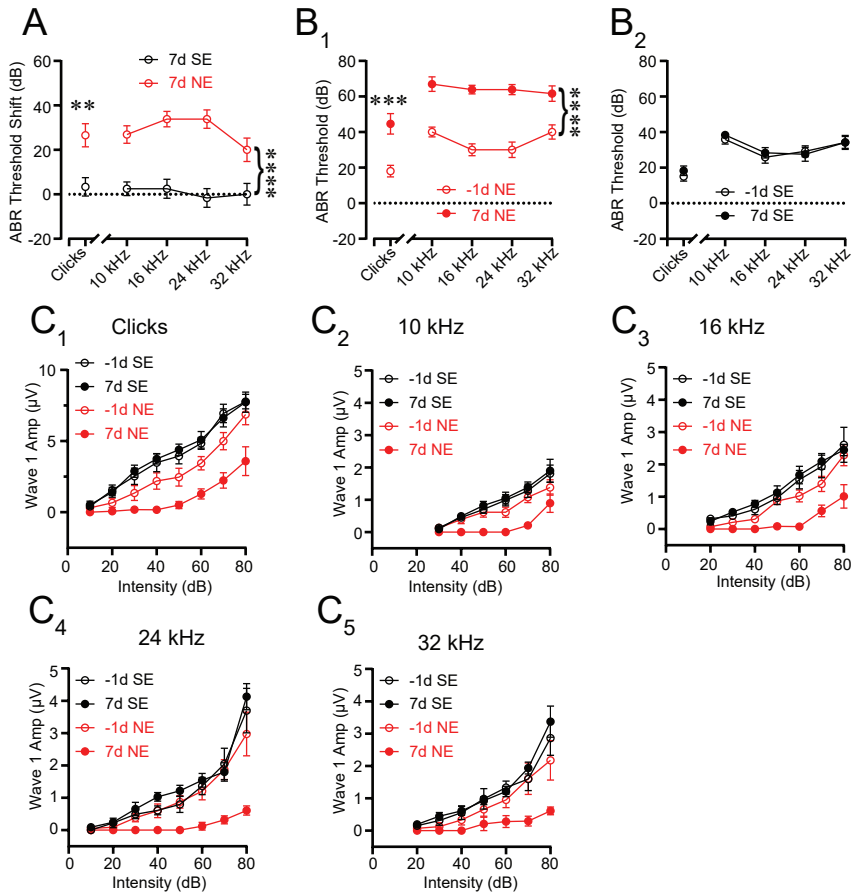
A
B1
B2
ABR Threshold Shift (dB)
ABR Threshold (dB)
7d SE
7d NE
-1d SE
-1d NE
Clicks
10 kHz
16 kHz
24 kHz
32 kHz
C1
C2
C3
C4
C5
Wave 1 Amp (µV)
Intensity (dB)

Figure S2

Table 1. Statistical values for Figures 1-7

Figure	Statistical test	Main effect 1	Main effect 2	Interaction effect	N (cells/mice)	Multiple comparison
1D	2-way ANOVA Bonferroni	Exposure: F (1,60) = 5.442 p = 0.023	Day: F (1,60) = 2.251 p = 0.1388	F (1,60) = 7.185 p = 0.0095	1d SE = 18/6 1d NE = 26/9 7d SE = 10/6 7d NE = 10/6	1d SE vs 1d NE, p = 0.0002 7d SE vs 7d NE, p > 0.9999 1d SE vs 7d SE, p > 0.9999 1d NE vs 7d NE, p = 0.0207
2A	Unpaired t-test		n/a		1d SE = 7/3 1d NE = 6/3	p = 0.0372
2C	Unpaired t-test		n/a		7d SE = 5/2 7d NE = 6/2	p = 0.6844
2E	Mann-Whitney test		n/a		1d SE = 18/6 1d NE = 26/9	p = 0.0042
2G	Unpaired t-test		n/a		7d SE = 10/6 7d NE = 10/6	p = 0.943
3A	2-way ANOVA Bonferroni	Exposure: F (1,85) = 0.1481 p = 0.7013	Day: F (1,85) = 2.261 p = 0.1364	F (1,85) = 0.3285 p = 0.5681	1d SE = 22/8 1d NE = 23/5 7d SE = 23/6 7d NE = 21/4	ns for all groups
3B	2-way ANOVA Bonferroni	Exposure: F (1,85) = 19.81 p < 0.0001	Day: F (1,85) = 9.395 p = 0.0029	F (1,85) = 6.912 p = 0.0102	1d SE = 22/8 1d NE = 23/5 7d SE = 23/6 7d NE = 21/4	1d SE vs 1d NE,p < 0.0001 1d SE vs 7d SE,p = 0.0007 1d NE vs 7d NE,p > 0.9999 7d SE vs 7d NE,p > 0.9999
3C	2-way ANOVA Bonferroni	Exposure: F (1,82) = 3.852 p = 0.0531	Day: F (1,82) = 4.345 p = 0.0402	F (1,82) = 0.0081 p = 0.9284	1d SE = 21/8 1d NE = 21/5 7d SE = 23/6 7d NE = 21/4	1d SE vs 1d NE,p > 0.9999 1d SE vs 7d SE,p = 0.9459 1d NE vs 7d NE,p = 0.7928 7d SE vs 7d NE,p = 0.8755
3D	2-way ANOVA Bonferroni	Exposure: F (1,80) = 3.733 p = 0.0569	Day: F (1,80) = 0.9135 p = 0.3421	F (1,80) = 1.256 p = 0.2657	1d SE = 21/8 1d NE = 19/5 7d SE = 23/6 7d NE = 21/4	1d SE vs 1d NE,p = 0.2285 1d SE vs 7d SE,p > 0.9999 1d NE vs 7d NE,p = 0.9321 7d SE vs 7d NE,p > 0.9999

3F	2-way ANOVA Bonferroni	Exposure: F (1,40) = 9.454 p = 0.0038	Current steps: F (2.431, 97.24) = 155.5 p < 0.0001	F (10,400) = 3.822 p < 0.0001	1d SE = 21/8 1d NE = 21/5	225 pA, p = 0.0291 250 pA, p = 0.0237 ns for all other groups
3H	2-way ANOVA Bonferroni	Exposure: F (1,42) = 2.644 p = 0.1114	Current steps: F (2.369, 99.49) = 208.3 p < 0.0001	F (10,420) = 0.9145 p = 0.5198	7d SE = 23/6 7d NE = 21/4	ns for all groups
4A	Mann-Whitney test		n/a		1d SE = 5/4 1d NE = 7/5	p = 0.6389
4C	Mann-Whitney test		n/a		7d SE = 10/6 7d NE = 10/6	p > 0.9999
4E	2-way ANOVA Bonferroni	Exposure: F (1,61) = 8.323 p = 0.0054	Day: F (1,61) = 0.05156 p = 0.8211	F (1,61) = 4.966 p = 0.0295	1d SE = 18/6 1d NE = 26/9 7d SE = 10/6 7d NE = 10/6	1d SE vs 1d NE,p = 0.0002 1d SE vs 7d SE,p > 0.9999 1d NE vs 7d NE,p = 0.4992 7d SE vs 7d NE,p > 0.9999
4G	2-way ANOVA Bonferroni	Exposure: F (1,32) = 1.877 p = 0.1802	Day: F (1,32) = 1.431 p = 0.2405	F (1,32) = 3.345 p = 0.0767	1d SE = 8/3 1d NE = 7/4 7d SE = 9/5 7d NE = 12/4	1d SE vs 1d NE,p > 0.9999 1d SE vs 7d SE,p > 0.9999 1d NE vs 7d NE,p = 0.229 7d SE vs 7d NE,p = 0.1151
5A	2-way ANOVA Bonferroni	Exposure: F (1,81) = 0.2748 p = 0.6015	Day: F (1,81) = 0.0164 p = 0.8984	F (1,81) = 1.411 p = 0.2384	1d SE = 21/6 1d NE = 21/5 7d SE = 20/5 7d NE = 23/6	ns for all groups
5B	2-way ANOVA Bonferroni	Exposure: F (1,81) = 1.545 p = 0.2174	Day: F (1,81) = 0.03028 p = 0.8623	F (1,81) = 1.545 p = 0.2174	1d SE = 21/6 1d NE = 21/5 7d SE = 20/5 7d NE = 23/6	ns for all groups
5C	2-way ANOVA Bonferroni	Exposure: F (1,81) = 3.793 p = 0.0549	Day: F (1,81) = 0.01358 p = 0.9075	F (1,81) = 0.2349 p = 0.6293	1d SE = 21/6 1d NE = 21/5 7d SE = 20/5 7d NE = 23/6	ns for all groups

5D	2-way ANOVA Bonferroni	Exposure: F (1,81) = 1.6 p = 0.2096	Day: F (1,81) = 0.1169 p = 0.7333	F (1,81) = 0.6401 p = 0.426	1d SE = 21/6 1d NE = 21/5 7d SE = 20/5 7d NE = 23/6	ns for all groups
5F	2-way ANOVA Bonferroni	Exposure: F (1,40) = 4.107 p = 0.05	Current steps: F (1.928, 77.11) = 769.6 p < 0.0001	F (14,560) = 0.9744 p = 0.4782	1d SE = 21/6 1d NE = 21/5	ns for all groups
5H	2-way ANOVA Bonferroni	Exposure: F (1,41) = 0.0221 p = 0.8827	Current steps: F (2.604, 106.8) = 716 p < 0.0001	F (14,574) = 1.067 p = 0.3853	7d SE = 20/5 7d NE = 23/6	ns for all groups
6B	2-Way ANOVA Bonferroni	Frequency: F (7, 11168) = 2.074 P=0.0428	Day: F (2, 11168) = 0.6583 P=0.5177	F (14, 11168) = 3.680 P<0.0001	-1d: 507/5 1d: 460/5 7d: 432/5	4 kHz: -1d vs 1d, p=0.1761; -1d vs 7d, p=0.5188; 1d vs 7d, p>0.9999 6 kHz: -1d vs 1d, p=0.0164; -1d vs 7d, p=0.1361; 1d vs 7d, p>0.9999 8 kHz: -1d vs 1d, p=0.4047; -1d vs 7d, p=2025; 1d vs 7d, p>0.9999 11 kHz: -1d vs 1d, p>0.9999; -1d vs 7d, p=0.8433; 1d vs 7d, p>0.9999 16 kHz: -1d vs 1d, p>0.9999; -1d vs 7d, p>0.9999; 1d vs 7d, p>0.9999 23 kHz: -1d vs 1d, p=0.2143; -1d vs 7d, p=0.4744; 1d vs 7d, p>0.9999 32 kHz: -1d vs 1d, p=0.0306; -1d vs 7d, p=0.0052; 1d vs 7d, p>0.9999 45 kHz: -1d vs 1d, p<0.0001; -1d vs 7d, p=0.0230; 1d vs 7d, p=0.2897
6C	2-Way ANOVA Bonferroni	Frequency: F (7, 15952) = 19.68 P<0.0001	Day: F (2, 15952) = 11.62 P<0.0001	F (14, 15952) = 2.777 P=0.0004	-1d:713/8 1d: 638/8 7d: 646/8	4 kHz: -1d vs 1d, p>0.9999; -1d vs 7d, p=0.0029; 1d vs 7d, p=0.0064 6 kHz: -1d vs 1d, p=0.4964; -1d vs 7d, p=0.0286; 1d vs 7d, p=0.7272 8 kHz: -1d vs 1d, p>0.9999; -1d vs 7d, p=0.0275; 1d vs 7d, p=0.1596 11 kHz: -1d vs 1d, p=0.0807; -1d vs 7d, p=0.0041; 1d vs 7d, p<0.0001 16 kHz: -1d vs 1d, p>0.9999; -1d vs 7d, p>0.9999; 1d vs 7d, p>0.9999 23 kHz: -1d vs 1d, p=0.4601; -1d vs 7d, p=0.2629; 1d vs 7d, p>0.9999 32 kHz: -1d vs 1d, p>0.9999; -1d vs 7d, p>0.9999; 1d vs 7d, p>0.9999 45 kHz: -1d vs 1d, p>0.9999; -1d vs 7d, p=0.4093; 1d vs 7d, p>0.9999
6D	2-Way ANOVA	Frequency: F (8, 8780) = 195.0 P<0.0001	Day: F (2, 8780) = 0.5215 P=0.5936	F (16, 8780) = 0.8117 P=0.6737	-1d: 507/5 1d: 460/5 7d: 432/5	n/a
		Frequency: F (8, 12876) = 166.4	Day: F (2, 12876) = 9.363	F (16, 12876) = 0.5219		bf-2: -1d vs 1d, p>0.9999; -1d vs 7d, p>0.9999; 1d vs 7d, p>0.9999 bf-1.5: -1d vs 1d, p>0.9999; -1d vs 7d, p>0.9999; 1d vs 7d, p>0.9999 bf-1: -1d vs 1d, p>0.9999; -1d vs 7d, p=0.4308; 1d vs 7d, p=0.1690

6E	2-Way ANOVA Bonferroni	P<0.0001	P<0.0001	P=0.9377	-1d:713/8 1d: 638/8 7d: 646/8	bf-0.5: -1d vs 1d, p=0.6740; -1d vs 7d, p=0.0304; 1d vs 7d, p=0.0007 bf: -1d vs 1d, p>0.9999; -1d vs 7d, p=0.1689; 1d vs 7d, p=0.1719 bf+0.5: -1d vs 1d, p>0.9999; -1d vs 7d, p=0.5826; 1d vs 7d, p=0.3420 bf+1: -1d vs 1d, p=0.9670; -1d vs 7d, p>0.9999; 1d vs 7d, p=0.6213 bf+1.5: -1d vs 1d, p>0.9999; -1d vs 7d, p=0.6451; 1d vs 7d, p>0.9999 bf+2: -1d vs 1d, p>0.9999; -1d vs 7d, p=0.8739; 1d vs 7d, p=0.8706
6F	2-Way ANOVA	Exposure: F(1, 316) = 1.004 P=0.3172	Day: F(2, 316) = 1.138 P=0.3217	F(2, 316) = 1.326 P=0.2670	-1d SE: 72/5 1d SE: 40/5 7d SE: 35/5 -1d NE: 99/8 1d NE: 36/8 7d NE: 40/8	n/a
6G	Bootstrap Bonferroni (see methods)		n/a		-1d SE: 507/5 1d SE: 460/5 7d SE: 432/5 -1d NE: 713/8 1d NE: 638/8 7d NE: 646/8	-1d SE vs -1d NE: p=0.6310 1d SE vs 1d NE: p=0.7120 7d SE vs 7d NE: p=0.3950 -1d SE vs 1d SE: p>0.9999 -1d SE vs 7d SE: p>0.9999 1d SE vs 7d SE: p>0.9999 -1d NE vs 1d NE: p>0.9999 -1d NE vs 7d NE: p>0.9999 1d NE vs 7d NE: p>0.9999
6H	2-Way ANOVA Bonferroni	Intensity: F (6, 9142) = 96.27 P<0.0001	Day: F (2, 9142) = 3.542 P=0.0290	F (12, 9142) = 2.509 P=0.0027	-1d: 438/5 1d: 460/5 7d: 411/5	20 dB: -1d vs 1d, p>0.9999; -1d vs 7d, p=0.8962; 1d vs 7d, p>0.9999 30 dB: -1d vs 1d, p>0.9999; -1d vs 7d, p>0.9999; 1d vs 7d, p>0.9999 40 dB: -1d vs 1d, p>0.9999; -1d vs 7d, p>0.9999; 1d vs 7d, p>0.9999 50 dB: -1d vs 1d, p=0.3758; -1d vs 7d, p=0.5527; 1d vs 7d, p=0.0131 60 dB: -1d vs 1d, p>0.9999; -1d vs 7d, p>0.9999; 1d vs 7d, p>0.9999 70 dB: -1d vs 1d, p=0.4815; -1d vs 7d, p=0.2436; 1d vs 7d, p>0.9999 80 dB: -1d vs 1d, p=0.0014; -1d vs 7d, p<0.0001; 1d vs 7d, p=0.6096
6I	2-Way ANOVA Bonferroni	Intensity: F (6, 12453) = 104.6 P<0.0001	Day: F (2, 12453) = 13.87 P<0.0001	F (12, 12453) = 5.445 P<0.0001	-1d:636/8 1d: 559/8 7d: 587/8	20 dB: -1d vs 1d, p>0.9999; -1d vs 7d, p>0.9999; 1d vs 7d, p>0.9999 30 dB: -1d vs 1d, p=0.7621; -1d vs 7d, p=0.7695; 1d vs 7d, p>0.9999 40 dB: -1d vs 1d, p=0.0008; -1d vs 7d, p=0.0001; 1d vs 7d, p>0.9999 50 dB: -1d vs 1d, p<0.0001; -1d vs 7d, p<0.0001; 1d vs 7d, p>0.9999 60 dB: -1d vs 1d, p=0.4984; -1d vs 7d, p=0.0208; 1d vs 7d, p=0.6272 70 dB: -1d vs 1d, p>0.9999; -1d vs 7d, p=0.6917; 1d vs 7d, p=0.4815 80 dB: -1d vs 1d, p>0.9999; -1d vs 7d, p=0.0264; 1d vs 7d, p=0.0068
		Exposure:	Day:			-1d SE vs -1d NE: p>0.9999

6J	2-Way ANOVA Bonferroni	F (1, 243) = 14.75 P=0.0002	F (2, 243) = 4.165 P=0.0166	F (2, 243) = 4.943 P=0.0079	-1d SE: 66/5 1d SE: 27/5 7d SE: 29/5 -1d NE: 71/8 1d NE: 31/8 7d NE: 25/8	1d SE vs 1d NE: p=0.0064 7d SE vs 7d NE: p=0.0016 -1d SE vs 1d SE: p=0.2749 -1d SE vs 7d SE: p>0.9999 1d SE vs 7d SE: p=0.4478 -1d NE vs 1d NE: p=0.3564 -1d NE vs 7d NE: p=0.0006 1d NE vs 7d NE: p=0.1410
6K	Bootstrap Bonferroni (see methods)	n/a			-1d SE: 438/5 1d SE: 460/5 7d SE: 411/5 -1d NE: 636/8 1d NE: 559/8 7d NE: 587/8	-1d SE vs -1d NE: p=0.8480 1d SE vs 1d NE: p=0.3810 7d SE vs 7d NE: p=0.6160 -1d SE vs 1d SE: p>0.9999 -1d SE vs 7d SE: p>0.9999 1d SE vs 7d SE: p>0.9999 -1d NE vs 1d NE: p>0.9999 -1d NE vs 7d NE: p>0.9999 1d NE vs 7d NE: p>0.9999
7B	2-Way ANOVA	Frequency: F (7, 9568) = 18.96 P<0.0001	Day: F (2, 9568) = 0.6797 P=0.5068	F (14, 9568) = 1.036 P=0.4130	-1d: 385/5 1d: 414/5 7d: 400/5	n/a
7C	2-Way ANOVA Bonferroni	Frequency: F (7, 6368) = 23.07 P<0.0001	Day: F (2, 6368) = 19.35 P<0.0001	F (14, 6368) = 1.933 P=0.0191	-1d: 268/4 1d: 235/4 7d: 296/4	4 kHz: -1d vs 1d, p>0.9999; -1d vs 7d, p=0.0865; 1d vs 7d, p=0.0981 6 kHz: -1d vs 1d, p>0.9999; -1d vs 7d, p=0.2231; 1d vs 7d, p=0.2338 8 kHz: -1d vs 1d, p>0.9999; -1d vs 7d, p=0.1674; 1d vs 7d, p=0.1308 11 kHz: -1d vs 1d, p=0.4992; -1d vs 7d, p=0.0003; 1d vs 7d, p=0.0537 16 kHz: -1d vs 1d, p>0.9999; -1d vs 7d, p=0.0393; 1d vs 7d, p=0.0055 23 kHz: -1d vs 1d, p=0.0204; -1d vs 7d, p=0.7009; 1d vs 7d, p=0.0003 32 kHz: -1d vs 1d, p=0.1851; -1d vs 7d, p>0.9999; 1d vs 7d, p=0.3827 45 kHz: -1d vs 1d, p=0.3300; -1d vs 7d, p=0.4330; 1d vs 7d, p>0.9999
7D	2-Way ANOVA	Frequency: F (8, 7831) = 99.52 P<0.0001	Day: F (2, 7831) = 0.5764 P=0.5619	F (16, 7831) = 0.5806 P=0.9009	-1d: 385/5 1d: 414/5 7d: 400/5	n/a
		Frequency: F (8, 5363) = 98.43	Day: F (2, 5363) = 12.03	F (16, 5363) = 1.842		bf-2: -1d vs 1d, p>0.9999; -1d vs 7d, p>0.9999; 1d vs 7d, p>0.9999 bf-1.5: -1d vs 1d, p>0.9999; -1d vs 7d, p>0.9999; 1d vs 7d, p>0.9999 bf-1: -1d vs 1d, p>0.9999; -1d vs 7d, p=0.0312; 1d vs 7d, p=0.0064

7E	2-Way ANOVA Bonferroni	P<0.0001	P<0.0001	P=0.0212	-1d: 268/4 1d: 235/4 7d: 296/4	bf-0.5: -1d vs 1d, p=0.7790; -1d vs 7d, p>0.9999; 1d vs 7d, p=0.1165 bf: -1d vs 1d, p=0.5393; -1d vs 7d, p<0.0001; 1d vs 7d, p<0.0001 bf+0.5: -1d vs 1d, p>0.9999; -1d vs 7d, p=0.9582; 1d vs 7d, p=0.1797 bf+1: -1d vs 1d, p>0.9999; -1d vs 7d, p>0.9999; 1d vs 7d, p=0.4891 bf+1.5: -1d vs 1d, p>0.9999; -1d vs 7d, p>0.9999; 1d vs 7d, p>0.9999 bf+2: -1d vs 1d, p>0.9999; -1d vs 7d, p>0.9999; 1d vs 7d, p>0.9999
7F	2-Way ANOVA Bonferroni	Exposure: F (1, 480) =17.67 P<0.0001	Day: F (2, 480) = 2.232 P=0.1084	F (2, 480) = 11.34 P<0.0001	-1d SE: 114/5 1d SE: 68/5 7d SE: 68/5 -1d NE: 111/4 1d NE: 54/4 7d NE: 71/4	-1d SE vs -1d NE: p>0.9999 1d SE vs 1d NE: p<0.0001 7d SE vs 7d NE: p=0.4043 -1d SE vs 1d SE: p=0.1443 -1d SE vs 7d SE: p>0.9999 1d SE vs 7d SE: p=0.0672 -1d NE vs 1d NE: p<0.0001 -1d NE vs 7d NE: p=0.3878 1d NE vs 7d NE: p=0.0145
7G	Bootstrap Bonferroni (see methods)		n/a		-1d SE: 385/5 1d SE: 414/5 7d SE: 400/5 -1d NE: 268/4 1d NE: 235/4 7d NE: 296/4	-1d SE vs -1d NE: p=0.098 1d SE vs 1d NE: p<0.0001 7d SE vs 7d NE: p=0.1750 -1d SE vs 1d SE: p>0.9999 -1d SE vs 7d SE: p>0.9999 1d SE vs 7d SE: p>0.9999 -1d NE vs 1d NE: p>0.9999 -1d NE vs 7d NE: p>0.9999 1d NE vs 7d NE: p=0.0360
7H	2-Way ANOVA	Intensity: F (6, 6279) = 44.38 P<0.0001	Day: F (2, 6279) = 0.2007 P=0.8182	F (12, 6279) = 0.9433 P=0.5019	-1d: 331/5 1d: 270/5 7d: 299/5	n/a
7I	2-Way ANOVA Bonferroni	Intensity: F (6, 4879) = 47.49 P<0.0001	Day: F (2, 4879) = 8.014 P=0.0003	F (12, 4879) = 2.900 P=0.0005	-1d: 226/4 1d: 222/4 7d: 252/4	20 dB: -1d vs 1d, p>0.9999; -1d vs 7d, p>0.9999; 1d vs 7d, p>0.9999 30 dB: -1d vs 1d, p=0.6319; -1d vs 7d, p=0.6348; 1d vs 7d, p>0.9999 40 dB: -1d vs 1d, p=0.1788; -1d vs 7d, p=0.0191; 1d vs 7d, p<0.0001 50 dB: -1d vs 1d, p>0.9999; -1d vs 7d, p=0.0541; 1d vs 7d, p=0.1216 60 dB: -1d vs 1d, p=0.0061; -1d vs 7d, p=0.1869; 1d vs 7d, p=0.5673 70 dB: -1d vs 1d, p=0.1120; -1d vs 7d, p=0.0510; 1d vs 7d, p>0.9999 80 dB: -1d vs 1d, p=0.5423; -1d vs 7d, p>0.9999; 1d vs 7d, p=0.2016

		Exposure:	Day:			-1d SE vs -1d NE: p>0.9999
		F (1, 368) = 11.23	F (2, 368) = 6.555	F (2, 368) = 3.496		1d SE vs 1d NE: p=0.0043
					-1d SE: 99/5	7d SE vs 7d NE: p=0.0148
					1d SE: 42/5	-1d SE vs 1d SE: p>0.9999
7J	2-Way ANOVA				7d SE: 50/5	-1d SE vs 7d SE: p=0.0096
	Bonferroni	P=0.0009	P=0.0016	P=0.0313	-1d NE: 83/4	1d SE vs 7d SE: p=0.0806
					1d NE: 49/4	-1d NE vs 1d NE: p=0.0068
					7d NE: 51/4	-1d NE vs 7d NE: p>0.9999
						1d NE vs 7d NE: p=0.0117
						-1d SE vs -1d NE: p=0.1970
						1d SE vs 1d NE: p=0.0450
					-1d SE: 331/5	7d SE vs 7d NE: p=0.0910
					1d SE: 270/5	-1d SE vs 1d SE: p>0.9999
	Bootstrap				7d SE: 299/5	-1d SE vs 7d SE: p>0.9999
7K	Bonferroni		n/a		-1d NE: 226/4	1d SE vs 7d SE: p>0.9999
	(see methods)				1d NE: 222/4	-1d NE vs 1d NE: p>0.9999
					7d NE: 252/4	-1d NE vs 7d NE: p>0.9999
						1d NE vs 7d NE: p=0.4230

Table 2. Statistical values for Supplemental Figures S1-S2

Figure	Statistical test	Main effect 1	Main effect 2	Main effect 3	Interaction effect	N (mice)	Multiple comparison
S1A clicks	Mann-Whitney test			n/a			p < 0.0001
S1A frequencies	2-way ANOVA Bonferroni	Exposure: F (1,47) = 235.5 p < 0.0001	Frequency: F (2.598, 122.1) = 2.156 p = 0.1055	n/a	F (3,141) = 3.93 p = 0.0099	1d SE = 24 1d NE = 25	p < 0.0001 for all groups
S1B1 clicks	Mann-Whitney test			n/a			p < 0.0001
S1B1 frequencies	2-way ANOVA Bonferroni	Exposure: F (1,48) = 388.5 p < 0.0001	Frequency: F (2.855, 137.1) = 27.68 p < 0.0001	n/a	F (3,144) = 3.839 p = 0.0111	-1d NE = 25 1d NE = 25	p < 0.0001 for all groups
S1B2 clicks	Mann-Whitney test			n/a			p = 0.5634
S1B2	2-way ANOVA Bonferroni	Exposure: F (1,46) = 0.264 p = 0.6099	Frequency: F (2.778, 127.8) = 25.46 p < 0.0001	n/a	F (3,138) = 0.8952 p = 0.4454	-1d SE = 24 1d SE = 24	ns for all groups
S1C1	3-way ANOVA	Exposure: F (1,52) = 20.93 p < 0.0001	Day: F (1,52) = 11.06 p = 0.0016	Intensity: F (2.25,117) = 393.2 p < 0.0001	F (7,364) = 8.586 p < 0.0001	-1d SE = 14 1d SE = 14 -1d NE = 14 1d NE = 14	n/a
S1C2	3-way ANOVA	Exposure: F (1,52) = 29.84 p < 0.0001	Day: F (1,52) = 16.36 p = 0.0002	Intensity: F (3.153,163.9) = 314.5 p < 0.0001	F (5,260) = 25.95 p < 0.0001	-1d SE = 14 1d SE = 14 -1d NE = 14 1d NE = 14	n/a
S1C3	3-way ANOVA	Exposure: F (1,52) = 31.2 p < 0.0001	Day: F (1,52) = 17.9 p < 0.0001	Intensity: F (2.026,105.3) = 253.9 p < 0.0001	F (7,364) = 8.467 p < 0.0001	-1d SE = 14 1d SE = 14 -1d NE = 14 1d NE = 14	n/a
S1C4	3-way ANOVA	Exposure: F (1,52) = 20.63 p < 0.0001	Day: F (1,52) = 16.83 p = 0.0001	Intensity: F (1.636,85.08) = 205 p < 0.0001	F (7,364) = 7.612 p < 0.0001	-1d SE = 14 1d SE = 14 -1d NE = 14 1d NE = 14	n/a
S1C5	3-way ANOVA	Exposure: F (1,52) = 28.62 p < 0.0001	Day: F (1,52) = 22.12 p < 0.0001	Intensity: F (2.136,111.1) = 253.8 p < 0.0001	F (6,132) = 11.39 p < 0.0001	-1d SE = 14 1d SE = 14 -1d NE = 14 1d NE = 14	n/a
S2A clicks	Mann-Whitney test			n/a			p = 0.0025

S2A frequency	2-way ANOVA Bonferroni	Exposure: F (1,23) = 32.09 p < 0.0001	Frequency: F (2.194, 50.46) = 3.018 p = 0.0532		n/a	F (3,69) = 3.018 p = 0.0356	7d SE = 12 7d NE = 13	10 kHz, p = 0.0003 16 kHz, p < 0.0001 24 kHz, p < 0.0001 32 kHz, p = 0.0444
S2B1 clicks	Mann-Whitney test		n/a					p = 0.001
S2B1 frequency	Mixed-effects Bonferroni	Exposure: F (1,24) = 47.89 p < 0.0001	Frequency: F (2.801, 65.36) = 3.873 p = 0.0148		n/a	F (3,70) = 3.069 p = 0.0334	-1d NE = 13 7d NE = 13	10 kHz, p < 0.0001 16 kHz, p < 0.0001 24 kHz, p < 0.0001 32 kHz, p = 0.0063
S2B2 clicks	Mann-Whitney test		n/a					p = 0.3261
S2B2 frequency	2-way ANOVA Bonferroni	Exposure: F (1,22) = 0.0599 p = 0.8089	Frequency: F (2.435, 53.56) = 7.606 p = 0.0006		n/a	F (3,66) = 0.3511 p = 0.7885	-1d SE = 12 7d SE = 12	ns for all groups
S2C1	3-way ANOVA	Exposure: F (1,20) = 27.6 p < 0.0001	Day: F (1,20) = 4.352 p = 0.0016	Intensity: F (1.954,39.07) =189 p < 0.0001		F (7,140) = 2.734 p = 0.0109	-1d SE = 6 7d SE = 6 -1d NE = 6 7d NE = 6	n/a
S2C2	3-way ANOVA	Exposure: F (1,20) = 16.63 p = 0.0006	Day: F (1,20) = 3.692 p = 0.069	Intensity: F (1.852,37.03) = 67.87 p < 0.0001		F (5,100) = 1.543 p = 0.1833	-1d SE = 6 7d SE = 6 -1d NE = 6 7d NE = 6	n/a
S2C3	3-way ANOVA	Exposure: F (1,20) = 19.92 p = 0.0002	Day: F (1,20) = 3.485 p = 0.0767	Intensity: F (2.058,41.15) = 79.58 p < 0.0001		F (6,120) = 1.949 p = 0.0784	-1d SE = 6 7d SE = 6 -1d NE = 6 7d NE = 6	n/a
S2C4	3-way ANOVA	Exposure: F (1,20) = 15.3 p = 0.0009	Day: F (1,20) = 3.958 p = 0.0605	Intensity: F (2.063,41.26) = 85.47 p < 0.0001		F (7,140) = 4.634 p = 0.0001	-1d SE = 6 7d SE = 6 -1d NE = 6 7d NE = 6	n/a
S2C5	3-way ANOVA	Exposure: F (1,18) = 13.38 p = 0.0018	Day: F (1,18) = 2.074 p = 0.167	Intensity: F (1.879,33.83) = 54.56 p < 0.0001		F (6,108) = 3.482 p = 0.0035	-1d SE = 6 7d SE = 6 -1d NE = 6 7d NE = 6	n/a